Journal of Iberian Geology (2021) 47:85–119
https://doi.org/10.1007/s41513-021-00162-3

RESEARCH PAPER

A genetic link between albitic magmas and IOCG mineralization in the Ossa Morena Zone (SW Iberia)

Jorge Carriedo[1] · Fernando Tornos[2] · Massimo Chiaradia[3] · Carmen Galindo[2,4]

Received: 5 August 2020 / Accepted: 18 January 2021 / Published online: 20 February 2021

Abstract

A detailed geological and isotopic study of the Colmenar deposit (Ossa Morena Zone, SW Iberia) shows that the magnetite-rich mineralization formed by complex magmatic-hydrothermal processes related to the crystallization of water-rich albite-magnetite igneous rocks derived from the crystallization of unusual melts formed during anatexis in a high temperature-low pressure metamorphic regime. The most likely protolith includes a sequence of iron-rich chemical sediments, amphibolite and possible meta-evaporites of early Cambrian age. The albite-magnetite rock occurs as up to 20 cm-thick dyke and breccia bodies and show complex immiscibility relationships with an albite-K-feldspar-quartz leucogranite. Iron-rich fluids exsolved during the crystallization of these melts are responsible of the formation of hydrothermal breccias and the widespread replacement of the hosting calc-silicate hornfels by a magnetite-ferroactinolite-albite assemblage along syn-mineralization shear zones. Geochronological data obtained for mineralization and related hydrothermal alteration points to a Variscan age (ca. 340 Ma), interpreted also as the age of the high-grade metamorphism driving anatexis at the Valuengo Metamorphic Complex. Despite the low Cu and Au contents, this mineralization shares features with the IOCG systems, which in other districts show a spatial relationship with albite-rich rocks, evaporites and pre-existing iron mineralization. The observations presented from Colmenar support an alternative genetic model with prospective implications for the Ossa Morena Zone that can be extrapolated to other IOCG belts worldwide.

Keywords IOCG · Magnetite · Geochronology · Radiogenic isotope geochemistry · Albitite

Resumen

El estudio geológico y geocronológico de detalle del depósito de Colmenar (Zona de Ossa Morena, SO Ibérico) muestra que la mineralización de magnetita se formó por procesos magmático-hidrotermales relacionados con la intrusión de un magma inusual (albita + magnetita) y rico en agua generado por anatexia en un ambiente metamórfico de alta temperatura y baja presión. El protolito más probable se corresponde con una secuencia de sedimentos químicos ricos en hierro, anfibolitas, y probablemente meta-evaporitas del Cámbrico Inferior. Estas rocas ricas en albita y magnetita se encuentran como brechas magmáticas y diques de hasta 20 centímetros de espesor, y presentan complejas relaciones de inmiscibilidad con leucogranitos ricos en albita, feldespato potásico y cuarzo. Los fluidos enriquecidos en hierro y exsueltos durante la cristalización de estos magmas fueron responsables de la formación de brechas hidrotermales soportadas por una matriz de ferroactinolita y magnetita, que también aparecen junto con albita remplazando rocas de silicatos cálcicos a favor de bandas de cizalla. La geocronología de la mineralización y alteración hidrotermal indica una edad Varisca (ca. 340 Ma), que se interpreta, su vez, como la edad del metamorfismo de alto grado responsable de los procesos de fusión parcial en el Núcleo Metamórfico de

Carmen Galindo: Deceased.

✉ Jorge Carriedo
j.carriedo@gmail.com

[1] Lundin Mining Corporation, 150 King Street West, Suite 2200, Toronto, ON M5H 1J9, Canada

[2] Instituto de Geociencias (CSIC-UCM), Dr Severo Ochoa 7, 28040 Madrid, Spain

[3] Section des Sciences de la Terre, University of Geneva, Rue des Maraichers 13, 1205 Geneva, Switzerland

[4] Departamento de Mineralogía y Petrología, Facultad de Ciencias Geológicas, Universidad Complutense de Madrid, 28040 Madrid, Spain

Valuengo. A pesar de sus bajos contenidos en Cu y Au, este estilo de mineralización comparte características con los sistemas tipo IOCG, que en otros distritos muestra relaciones espaciales con albititas, evaporitas, y mineralizaciones de hierro preexistentes.Las observaciones en Colmenar soportan un modelo genético alternativo con implicaciones prospectivas para la zona de Ossa Morena, y que es extrapolable a distritos IOCG en otras partes del mundo.

Palabras clave IOCG · Magnetita · Geocronología · Geoquímica de isotopos radiogénicos · Albitita

1 Introduction

A debate exists on the genesis of the abundant iron deposits in the Ossa Morena Zone (Fig. 1), showing different morphologies, relationships with host rocks and plausible origins. Some of them have been interpreted as exhalative synsedimentary mineralization coeval with Cambrian volcanism subsequently metamorphosed (Doetsch 1967; Locutura et al. 1990). However, the frequent presence of coarse-grained calcsilicate-rich assemblages, the presence of epigenetic replacing textures and the spatial relationship with major shear zones and Variscan intrusive rocks have served as an argument for a magmatic-hydrothermal origin, being classified as skarns (Casquet and Tornos 1991; Febrel 1970; Sanabria et al. 2005; Cuervo et al. 1996) or IOCG type mineralization (Tornos et al. 2003; Tornos and Casquet 2005; Tornos and Carriedo 2006; Carriedo and Tornos 2010).

Other authors have proposed a link between exhalative and epigenetic mineralization (Baeza et al. 1978; Vázquez and Fernández 1976; Ruiz García 1975), where a syngenetic stratiform mineralization would be assimilated by magmas and part of the iron subsequently incorporated into the fluid phase, exsolved during its crystallization and reacting with the surrounding carbonate rocks to give the replacive skarn mineralization.

The Colmenar deposit is one of multiple examples of iron-rich mineralization widespread across the Ossa Morena zone. It belongs to the San Guillermo-Colmenar-Santa Justa mining complex, around Valuengo water dam (Badajoz, Spain), and exploited for iron by Minera del Andevalo S.A. from 1956 to 1977, using underground and open pit methods. Magnetite was the main ore mineral, with average grades around 45.5% Fe, but high alkali contents caused the cessation of production (Vázquez et al. 1980; Vázquez and Fernández 1976).

This work is focused on a detailed geological and isotopic study of the Colmenar deposit, where various types of mineralization are seemingly with igneous rocks within a shear band.

2 General geological context

The Ossa-Morena Zone, within the European Variscan Belt (Fig. 1), represents a continental block part of the Gondwana northern margin (Robardet, 2003; Arenas et al. 2016). This region records a complex evolution including the Neoproterozoic Cadomian orogeny (ca 650–550 Ma), and a subsequent (ca 510–480 Ma) Cambro-Ordovician extension (Eguiluz et al. 2000; Expósito 2000; Expósito et al. 2003; Sánchez-García et al. 2003; 2010; Chichorro et al. 2008; Pereira et al. 2009; Cambeses et al. 2017). Later, during Variscan orogeny, the Ossa Morena Zone was deformed under a collisional regime, reflected in both north and south margins registering convergence. (Bard and Moine 1979; Abalos Villaro et al. 1991; Arenas et al 2016 and references therein).

Two main magmatic events are well discriminated at the Ossa Morena Zone (Fig. 1); (i) a lower Cambrian rifting stage at ca 530–490 Ma (Sánchez-García et al. 2003, 2010), and (ii) a short-lived intra-orogenic extensional event during the main Variscan collision at ca 350–330 Ma (Apraiz and Eguiluz, 2002; Simancas et al. 2003; Cambeses, 2015).

Low-grade regional metamorphism affects the Ossa Morena Zone in the greenschist facies, with localized MT/HT-LP metamorphism. These higher-grade metamorphic domains commonly present migmatization process and have been attributed in several sectors as contemporaneous with the Variscan magmatic event (Ordóñez 1998; Pereira et al. 2009; Díaz Azpiroz et al. 2004, 2006).

Most of the ore deposits of the Ossa Morena Zone, including Colmenar deposit, are in the Olivenza-Monesterio Belt (Locutura et al. 1990; Tornos et al. 2004), that broadly coincides with the Olivenza-Monesterio antiform, a regional Variscan structure with NW–SE trend and SW vergence.

The Colmenar deposit is in a structurally complex area between the NW margin of the Valuengo Metamorphic Complex (HT/LP) and the eastern contact of the Variscan Brovales Pluton (Fig. 2), along a North–South trending ductile/brittle shear zone of sinistral component.

3 The Valuengo metamorphic complex

The Valuengo metamorphic complex covers an area of 28 km^2 with an ellipsoidal NNE trending shape (Fig. 2) and is dominantly interpreted as an antiformal dome-type structure (Coullaut et al. 1981; Apraiz and Eguiluz 1996), whose core includes high-grade metamorphic rocks with widespread migmatization and formation of anatectic granitoids. A key characteristic of the Valuengo metamorphic complex is the presence of abundant intrusions of albitite surrounding the core of the structure (Fig. 2).

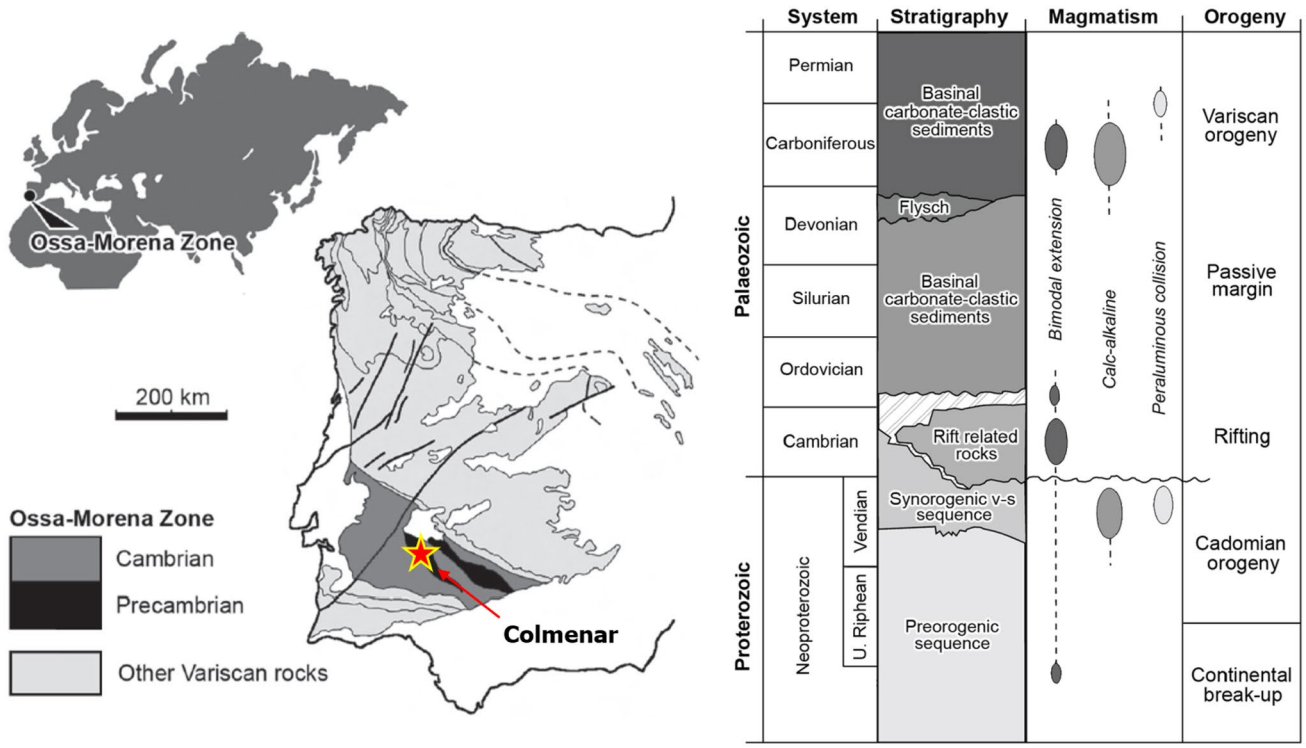

Fig. 1 location of Colmenar within the Ossa Morena Zone at the Iberian Massif (centre; modified from Julivert et al. 1974) and Eurasia (top left). The chart shows the stratigraphic succession and temporal correlation of the main igneous and tectonic events of the Ossa Morena Zone, (right; adapted from Quesada 1992)

The Colmenar deposit is hosted by Las Mayorgas Formation (Coullaut et al. 1981), a highly deformed lower Cambrian sequence of general N/NE-S/SW orientation, dominated by calcsilicate-rich rocks and marbles. Underlying the Las Mayorgas Formation is the Valuengo Gneissic-Migmatitic Formation (Coullaut et al. 1981), a high-grade metamorphic unit in sharp contrast with the regional low grade greenschist facies. This metamorphic core is bounded by low angle extensional structures subparallel to the regional foliation. These structures abruptly juxtapose underlying rocks with metamorphism in the amphibolite facies with overlaying meta-sediments and volcanic rocks in the greenschist facies (Fig. 2). These observations suggest an exhumed core complex linked with extension associated with gravitational collapse of a swelled crust, as in other sectors of the Ossa Morena Zone (Apraiz and Eguiluz 2002).

The Valuengo metamorphic complex has been also interpreted to form during thin skinned tectonics, in which the high metamorphic core would be related to the hinge of a large recumbent fold of Variscan age, folding of the shear bands surrounding the migmatitic core, and later intersected by a system of southwards thrusts and a late folding (Expósito et al. 2003).

Its main distinctive feature is the high metamorphic grade, which contrasts with the low-grade regional metamorphism that dominates in the Ossa Morena Zone, and that almost never overcomes greenschist facies conditions (López-Munguira and Nieto 2004). High temperature and low-pressure metamorphic conditions have been described in this area, with development of partial melting processes under conditions up to 10–12 kb at maximum temperatures of 600–650 °C, and with a later thermal peak maximum at around 700 °C and 8 kb (Apraiz and Eguiluz 1996).

The age of metamorphism and deformation is still under debate (Expósito et al. 2003; Apraiz and Eguiluz 1996, 2002; Apraiz 1998; Fernández et al. 1981). The existing U–Pb dating of an orthogneiss from the north-eastern limit of the Valuengo dome, using the zircon sequential evaporation method (Kober 1986, 1987), has given an age of 532 ± 5 Ma (Expósito et al. 2003). Based on this geochronology, these authors attribute the high-grade metamorphism to a pre-Variscan tectonometamorphic event, associated with the Cambrian rifting (Expósito et al. 2003).

An earlier U–Pb dating on the orthogneiss using the same zircon method has given a similar age of 535 ± 5 Ma (Montero et al. 2000) and is consistent with the interpretation that supports a Cambrian age for the dome; however, in the same study with the same zircon method, the nearby amphibolite has yielded an age of 342 ± 4 Ma (Montero et al. 2000). This late age is similar to that obtained for the metamorphism of the Lora del Rio Metamorphic area (ca. 340 Ma; Ordóñez 1998), another high-grade metamorphic

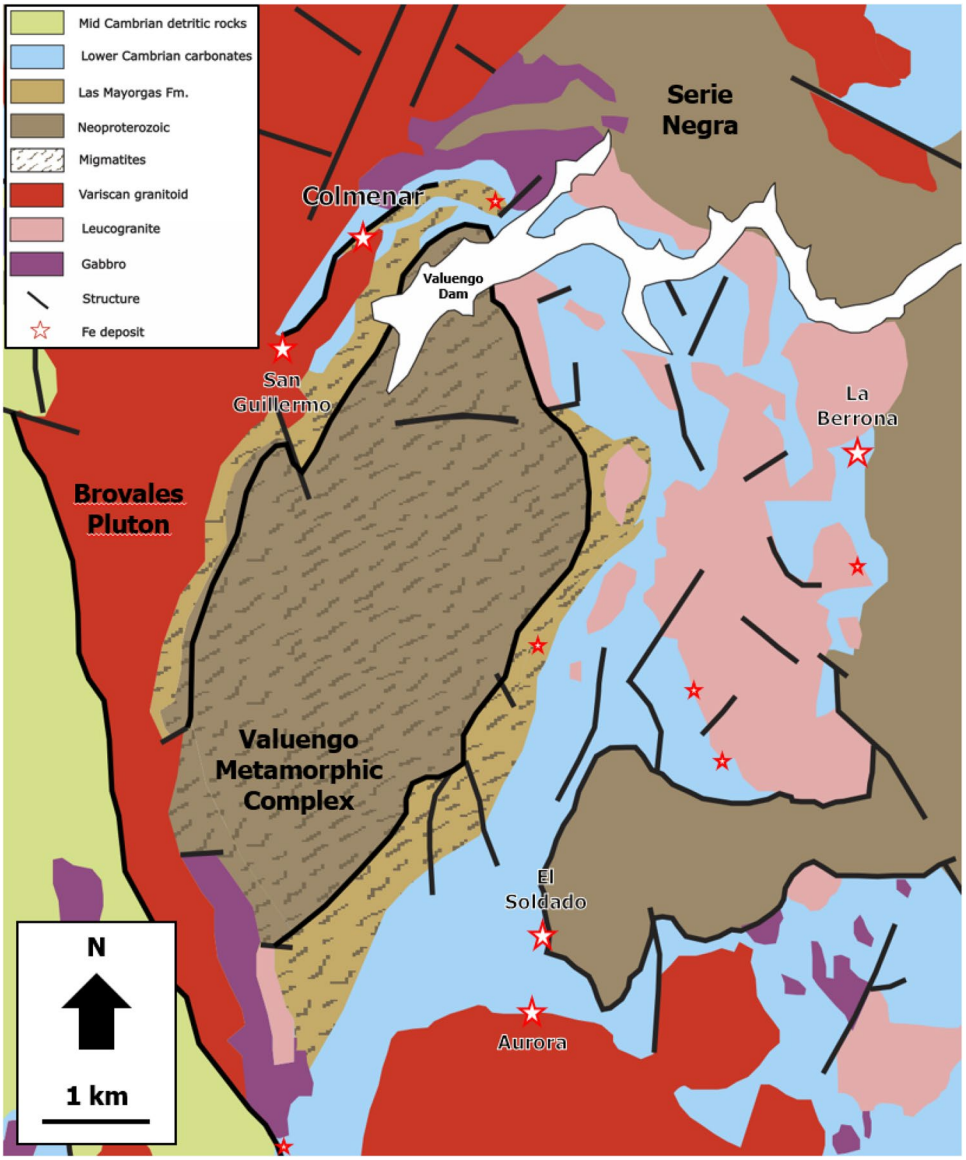

Fig. 2 Geological map with the location of Colmenar deposit within the Valuengo Metamorphic Complex. Modified from Apraiz et al. (1996), Quesada & Sánchez-García (2002) and Expósito et al. (2003)

area within the Ossa Morena Zone that has been correlated by some authors to the Valuengo metamorphic complex (Apraiz and Eguiluz 2002; Apraiz 1998). Therefore, they interpret that these spatially restricted zones of high-grade regional metamorphism would be linked to extensional processes in the late stages of the Variscan orogeny (Apraiz and Eguiluz 1996, 2002; Eguiluz et al. 2000), dated in other sectors of the Ossa Morena (Ordóñez 1998; Pereira et al. 2012).

Discontinuous stratabound magnetite-rich lenses can be followed for up to five kilometers around the Valuengo metamorphic core (Vázquez et al. 1980; Coullaut et al. 1980). There are multiple iron occurrences and several historic mines like San Guillermo, Colmenar-Santa Bárbara and Santa Justa (Vázquez et al. 1980; Sanabria et al. 2005; IGME 2006), or La Berrona, where the magnetite-rich mineralization replaced limestone and calcsilicate rocks around an albitic intrusion (IGME 1979; 2006; Tomé 2012; Coullaut et al. 1980).

4 Stratigraphy

The protolith for the high metamorphic rocks conforming the Valuengo metamorphic complex have been interpreted as volcanoclastic sequences from the Valuengo Gneissic-Migmatitic Formation and Las Mayorgas Formation, the later host of Colmenar mineralization.

The Valuengo formation crops out in an approximate area of 3 × 5 km (Fig. 2). It is dominated by migmatitic gneiss, shale, quartz-schist, decimeter-thick intercalations of recrystallized carbonates and irregular intercalations of basic rocks transformed into amphibolites (Coullaut et al. 1981). The

stratigraphic thickness of this formation exceeds one hundred meters and has an unknown footwall (Apraiz and Eguiluz 1996), and interpreted as the metamorphic equivalent of a distal volcanoclastic sequence, regionally correlated with the Bodonal-Cala Complex (Eguiluz et al. 1992). This correlation is based on the presence of a level of mineralized carbonate rocks and a level of "porphyry tuffs", analogous to those described in the basal sections of the Bodonal-Cala Complex (Eguiluz et al. 1983; Eguiluz 1987). This is interpreted as part of the upper Cadomian calc-alkaline volcanism around 514 Ma (Eguiluz et al. 1999; Ordóñez 1998).

The Valuengo Formation is overlain by the Las Mayorgas Formation (Coullaut et al. 1981), cropping out around the core of the dome (Fig. 2). This formation is made up of decametric levels of coarse-grained meta-arkoses alternating with shales and abundant calc-silicate rocks, amphibolites, limestones, porphyritic gneiss and magnetite-rich exhalative levels (Coullaut et al. 1981). Close to the stratigraphic hanging wall, there is a discontinuous marker horizon conformed by limestone, dolostone and calc-silicate rocks up to a few tens of meters in thickness. This level hosts frequent stratiform magnetite bodies and is the preferred horizon for the development of iron-rich skarns (Coullaut 1979).

The Las Mayorgas Formation has been interpreted as a calc-alkaline island arc volcanoclastic sequence equivalent to the Malcocinado Formation, (Apraiz and Eguiluz 1996; Apraiz 1998; Expósito 2000; Expósito et al. 2003), dated as Neoproterozoic-Lower Cambrian age and widely exposed along the Ossa Morena Zone.

Overlying Las Mayorgas Formation there is a carbonate sequence, up to 150 m in thickness, of lower Cambrian age (Coullaut et al. 1981), correlated with the abundant carbonate rocks at the base of the Cambrian found throughout the Ossa Morena area (San José et al. 2004).

Rocks of the uppermost Las Mayorgas Formation show a penetrative foliation and mineral stretch lineation, consistent with the presence of a major ductile–brittle shear zone. The carbonate package at Colmenar shows low-grade metamorphic conditions, as opposed to the high-grade metamorphism described for the underlying rocks and representing an important metamorphic jump along the stratigraphic sequence in few meters.

Shearing evidences are well exposed at Colmenar mine, with the mineralization being controlled by a subvertical N30E shear zone (Colmenar Shear Band). Its extension to the south is truncated by the intrusion of the Brovales Pluton, whereas it is not easy to follow to the north given the scarcity of outcrops, although some authors have extrapolated its extension several kilometers up to the Burguillos del Cerro Pluton (Tornos et al. 2002).

West of the Colmenar mine, the carbonate unit is truncated by the Brovales Pluton, that extends for several kilometers on a N–S orientation (Fig. 2). This Variscan tonalitic-granodioritic body of calc-alkaline nature has been dated at 340 ± 7 Ma (Montero et al. 2000). It shows evidences of diverse magmatic pulses clearly syn-tectonic with the Variscan deformation (Eguiluz et al. 2004). In the northern sector, the Brovales Pluton shows a N120° E foliation dipping 30° NE and probably corresponding to the west extension of the Monesterio Thrust, a regional structure with a similar tectonic pattern (Eguiluz et al. 2004). The southern sector of the intrusion lacks internal fabric but the contacts with the host rocks are controlled by sinistral shears (Eguiluz et al. 2004).

5 Mineralization host rocks at Colmenar

The Las Mayorgas Formation is the main host for the iron-rich mineralization. Here, consists of ca. 120 m of schists and shales with lenses of amphibolite and felsic orthogneiss and a very continuous level of calcsilicate rocks totally hydrothermally replaced (Fig. 3).

5.1 Schists and amphibolites

Schists dominate in the northern part of the deposit (Fig. 3) as dark grey homogeneous levels with abundant discontinuous intercalations of amphibolites, presumably the product of the regional metamorphism of mafic igneous rocks, as observed in the Valuengo Formation (Coullaut et al. 1981). The schist is composed by quartz, potassium feldspar, plagioclase, and biotite with accessory almandine, zircon, apatite and titanite. Some domains present variable concentrations of magnetite between 1 and 10%. These high contents of primary magnetite are interpreted as linked to possible exhalative levels like those cited in nearby areas (Dupont 1979). These rocks usually have little evidence of hydrothermal alteration, restricted to incipient feldspar sericitization and hornblende replacement by epidote.

The amphibolite is dominated by oriented fine-grained ferrohornblende with lesser amounts of plagioclase and magnetite. This rock is similar to undeformed, more coarse-grained gabbro and likely it is its deformed equivalent. However, other studies propose that the amphibolite is derived from mafic flows of the Early Cambrian volcanism (Coullaut et al. 1981).

5.2 Limestones and calcsilicate rocks

Calcium rich rocks are abundant at eastern sectors of Colmenar open pit, near the contact between Las Mayorgas Formation and the eastern tonalite, and along the eastern contact of main mineralized zone (Fig. 3). These rocks usually present an intense hydrothermal alteration that obliterates their primary textures and paragenesis; outside the mineralized zones calc-silicate rocks are scarce. They usually show

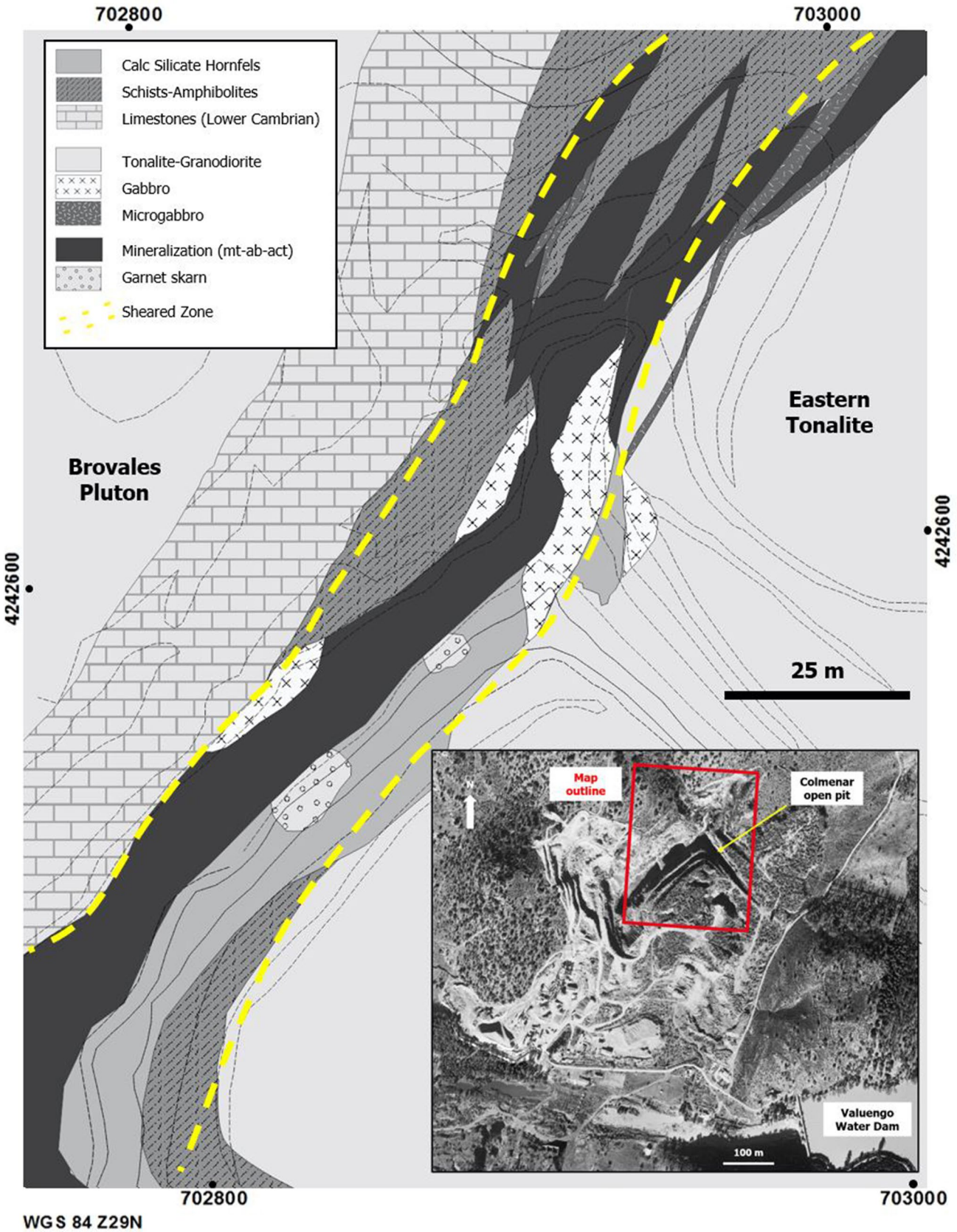
702800
703000
Calc Silicate Hornfels
Schists-Amphibolites
Limestones (Lower Cambrian)
Tonalite-Granodiorite
Gabbro
Microgabbro
Mineralization (mt-ab-act)
Garnet skarn
Sheared Zone
Brovales Pluton
Eastern Tonalite
4242600
4242600
25 m
Map outline
Colmenar open pit
Valuengo Water Dam
100 m
702800
703000
WGS 84 Z29N

◂**Fig. 3** Geological mapping from Colmenar open pit showing the distribution of the main mined orebody developed by hydrothermal replacement alternating schists and calc-silicate rocks of rocks from Las Mayorgas Fm. This sequence is limited to the west by a younger carbonate Fm. intruded by Brovales Pluton, whose eastern tonalitic apophysis intrudes along the eastern contact of Las Mayorgas Fm.

a fine-grained compositional layering (Fig. 4a), with variable abundances of diopside, scapolite, oligoclase-andesine, clinoamphibole, epidote and magnetite. There are minor relicts of limestone dominated by calcite with minor amounts of detrital quartz (Fernández et al. 1981).

The Early Cambrian carbonatic sequence occur as a 20–100 m package of recrystallized limestone and minor dolostones along western contact at Colmenar. To the south, this carbonate package constitutes the host rock for the skarn-type mineralization at Santa Bárbara mine.

5.3 Igneous rocks

Detailed mapping of the Colmenar deposit shows that there are three main types of igneous rocks, including tonalite, gabbro and small amounts of albitite. Albite-rich intrusions are abundant in the Valuengo sector and, due to its uniqueness and the metallogenic implications observed, they are described in detail later.

The eastern tonalite is exposed with an elongated morphology along a N30E trend along less than one kilometer, with a maximum width of 200 m. Its non-exposed southern contact has been extrapolated as an apophysis of the nearby Brovales Pluton (Sanabria et al. 2005; Expósito et al. 2003). Like the Brovales Pluton, it has a tonalitic-granodioritic composition and includes an assemblage of quartz, plagioclase, potassium feldspar, and biotite, with clino-amphibole, zircon, apatite and allanite as accessory minerals.

Texturally it shows a marked anisotropy (Fig. 4b) with frequent syn-magmatic SC-type structures defined by the orientation of biotite and clinoamphibole crystals. The internal anisotropy becomes more penetrative and subvertical to the west, approaching the zone of maximum deformation and mineralization. Although most of the plagioclase is albitized, it is in this sector closer to mineralization where the tonalite is most clearly altered.

Within the shear band and in the vicinity of the deposit, there are abundant bodies of gabbro with a massive isotropic texture despite being located inside the Colmenar Shear Zone (Fig. 3). Mineralogically they consist of clinoamphibole (ferrohornblende-ferrotschermakite) and plagioclase (albite to andesine; locally to residual bytownite), with a coarse-grained equigranular mosaic texture. Accessory minerals are quartz, biotite, apatite and variable contents of ilmenite and pyrite (Fig. 4c). This gabbro has been traditionally interpreted of Cambrian age (Coullaut et al. 1981).

6 Albitite

A relevant aspect in the Colmenar mine is the presence of rocks formed almost exclusively by albite with variable concentrations of magnetite. These rocks occur in three different ways: (i) As leucocratic domains in migmatized zones; (ii) As a coarse matrix of breccias; and, (iii) in swarms of centimeter- to decimeter-sized dykes. In detail, the three types of albitite seem to be broadly coeval, showing gradual transitions between them.

6.1 Albite-rich leucocratic domains

Clear evidences of partial melting and migmatite formation are observed at alternances of schist and amphibolite within the Mayorgas Formation at Colmenar (Fig. 5a, b). Some areas show metatexites or incipient migmatization (Mehner 1968), in which the leucosome is restricted to millimeter-sized bands, or at most with mm-cm albitic patches, elongated subparallel to the foliation. Other areas are characterized by the development of diatexites, with well-defined leucosome domains with schlieren and nebulitic structures (Mehner 1968). Here, leucosome domains are intermingled with darker fine- to medium grained domains or melanosome/restite, dominated by recrystallized biotite and relict mixed domains or paleosome (Mehner 1968; Schmid et al. 2007).

Fine-grained textures are observed in the incipient leucosome along mm to centimeter bands, as opposed to grain sizes of up to 1 cm in well-developed leucosome domains. In the latter, leucosome shows an undeformed mosaic texture, suggesting that the migmatization process is subsequent to the regional penetrative deformation.

Plagioclase is the dominant mineral (albite-oligoclase), with variable amounts of magnetite, actinolite, titanite and apatite. A relevant aspect is the abundance of apatite in some leucosome areas, which can give rise to form millimetric-centimetric discrete bands (Fig. 5c) of massive apatite or intergrown with albite and magnetite.

6.2 Albite-supported breccias

Close to the mineralization, when leucosome is abundant, there are some unusual breccias that include angular and heterometric, cm-sized, clasts of gabbro and, to a lesser extent, amphibolite and shale. Clasts are supported by a coarse-grained albite-oligoclase groundmass, like that of the leucosome (Fig. 5d), with plagioclase crystals that can exceed one centimeter. Locally, myrmekites of plagioclase and quartz

Fig. 4 **a** Calc silicate rocks from Las Mayorgas Fm. showing a tipical banded texture attributed to sedimentary in origin. These rocks are hydrothermally replaced by an assemblage dominated by actinolite and magnetite and interpreted as the main host of mineralization at Colmenar; **b** Eastern tonalite outcropping at Colmenar deposit, with a distinctive layered texture observed close to the contact with Colmenar mineralization; **c** textural detail of the gabbro, dominated by plagioclase and hornblende with accessory opaque minerals dominated by ilmenite and pyrite. The upper domain corresponds to a coarse-grained plagioclase replaced aby an associaton of sericite and epidote (left not analized light, right analized light, 3.2×)

are characteristic. Inter-grown with plagioclase there are varying amounts of magnetite, actinolite, titanite (locally very abundant) and zircon, with minor quartz and apatite.

Like the leucosome domains, the albitic matrix shows no evidence of deformation or preferred orientation and the foliation at the breccia clasts is truncated (Fig. 5e), corroborating a post-tectonic brecciation and albite crystallization.

No clear evidences of migmatization are observed in the breccia clasts, suggesting that the albitic melt (discussed below) was injected into the brittle rocks by migration from the nearby migmatitic areas. Clasts are unaltered and only locally there is a millimeter-to-centimeter reaction edge with replacement of the original hornblende by an association, chlorite, and epidote (Fig. 5f).

6.3 Albitic dykes

There are abundant albitic dykes with thicknesses from some cm to one meter, whose orientation and distribution are partially controlled by the host rock. When the dykes are hosted by the gabbro, they do not follow a preferred orientation and the dykes present a stockwork-like distribution (Fig. 6). These dykes present straight and sharp contacts with the host rock, and lack of alteration sealvage.

When associated with more ductile-deformed or anisotropic rocks such as the mineralized calc-silicate hornfels, the dikes are parallel to the tectonic foliation. They are generally smaller in size, not exceeding the centimeter in thickness, and show abutted and stretched shapes with lobed edges interpreted as due to crystallization in a syn-tectonic environment (Fig. 7a).

The main assemblage of these dykes consists of albite and magnetite (Fig. 7b), with marked internal mineralogical heterogeneities within a single dyke (Fig. 6). The albite-magnetite rock punctually shows irregular but sharp contacts with a leucogranite domain with albite-oligoclase and minor contents of K feldspar, actinolite, biotite, quartz and titanite but lacking magnetite (Fig. 6, 7c).

Textures are also variable, from coarse-grained heterometric domains to fine-grained aplitic textures, but not necessary correlating with a specific mineralogy. Some textures include bands defined by the alternance magnetite versus albite contents, unidirectional solidification textures (Breiter et al. 2005; London 1992; Shannon et al. 1982; Fig. 7d) or stockscheider structures (Nesen 1981).

These observed heterogeneities, their erratic distribution within the same dyke structure and the lack of clear signs of hydrothermal alteration, points to crystalized immiscible melts, close to pneumatolytic conditions, as a possible mode of origin.

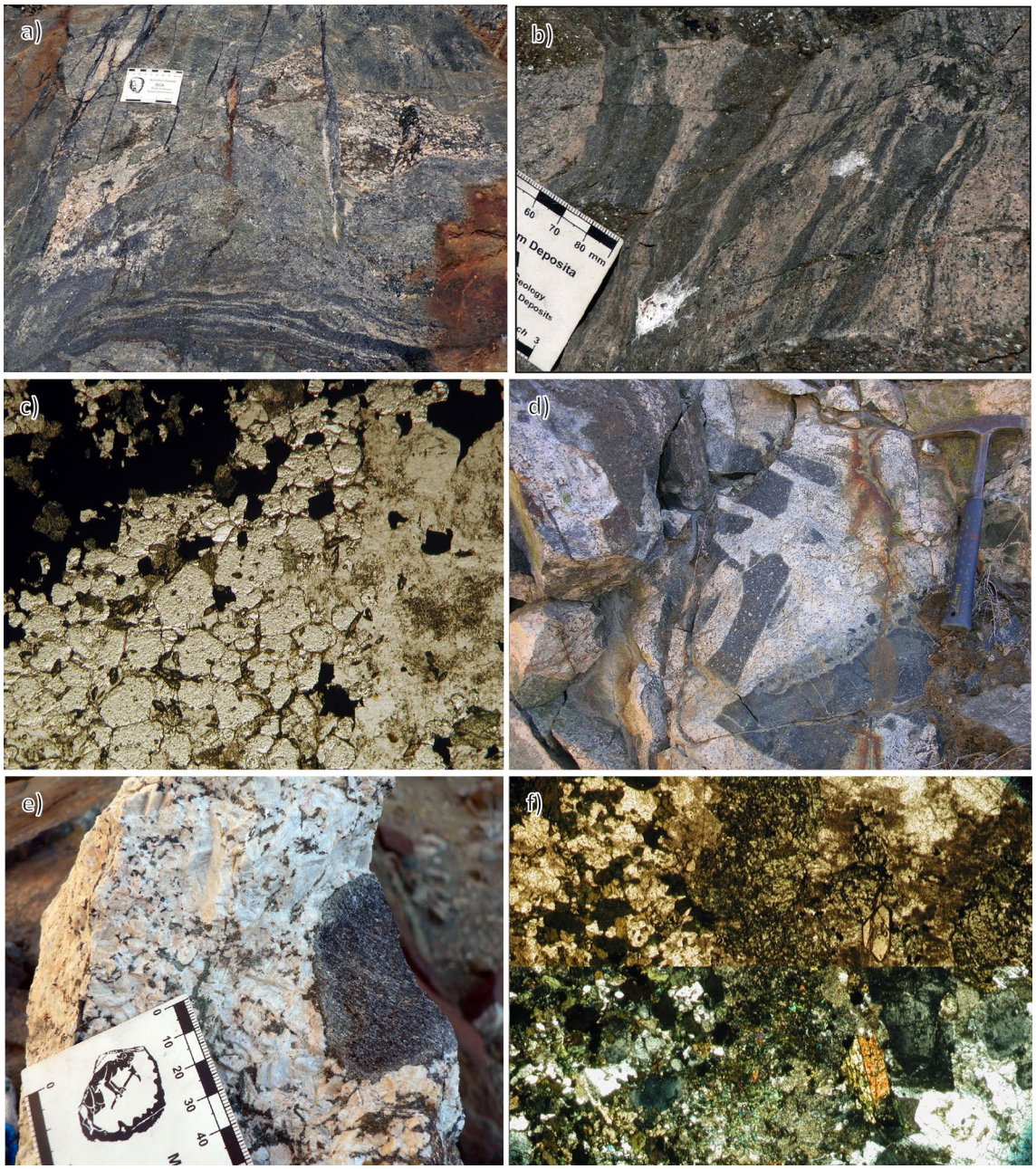

Fig. 5 **a**, **b** Migmatites over a schist-amphibolite domain at northern sectors in Colmenar. Whitish coarser grain domains represent leucosome domains subparallel to tectonic foliation, composed by different proportions of albite and magnetite. Alternating darker domains correspond to melanosome biotite rich domains or paleosome domains, in both cases following the same structural trend; **c** detail of a leucosome showing a discrete apatite rich domain, represented by the high relief crystals. In contact at the left with a magnetite-actinolite domain, and to the right with an albite domain partially sericitized. Observed abundand intergrown titanites at both albite and apatite domains, with their singular bipyramidal shapes (not analized light, 5×); **d** matrix supported breccia at northern sector of Colmenar. It shows decimetric gabbro clasts with sharp and straight borders without clear dominant orientation, supported by a coarse-grained albitic matrix; **e** Brecciation detail of the albitic matrix with minor amounts of amphibole and titanite, supporting a foliated clast of amphibolite. Brecciation crosscuts the foliation planes with no evidences of deformation within the albitic matrix indicating a postectonic brecciation process. Only a millimetric reaction border is developed at the amphibolite clast, without signs of intense alteration; **f** Breccia detail of the contact between an amphibolite clast (left) supported by an albite rich matrix (right). In between, the millimetric reaction border transform primary hornblende from the amphibolite into chlorite and epidote and minor actinolite. A well-developed bypiramidal titanite crystal can be observed at the albitic domain in close contact with the reaction border (up not analyzed light, down analyzed light, 3.2×)

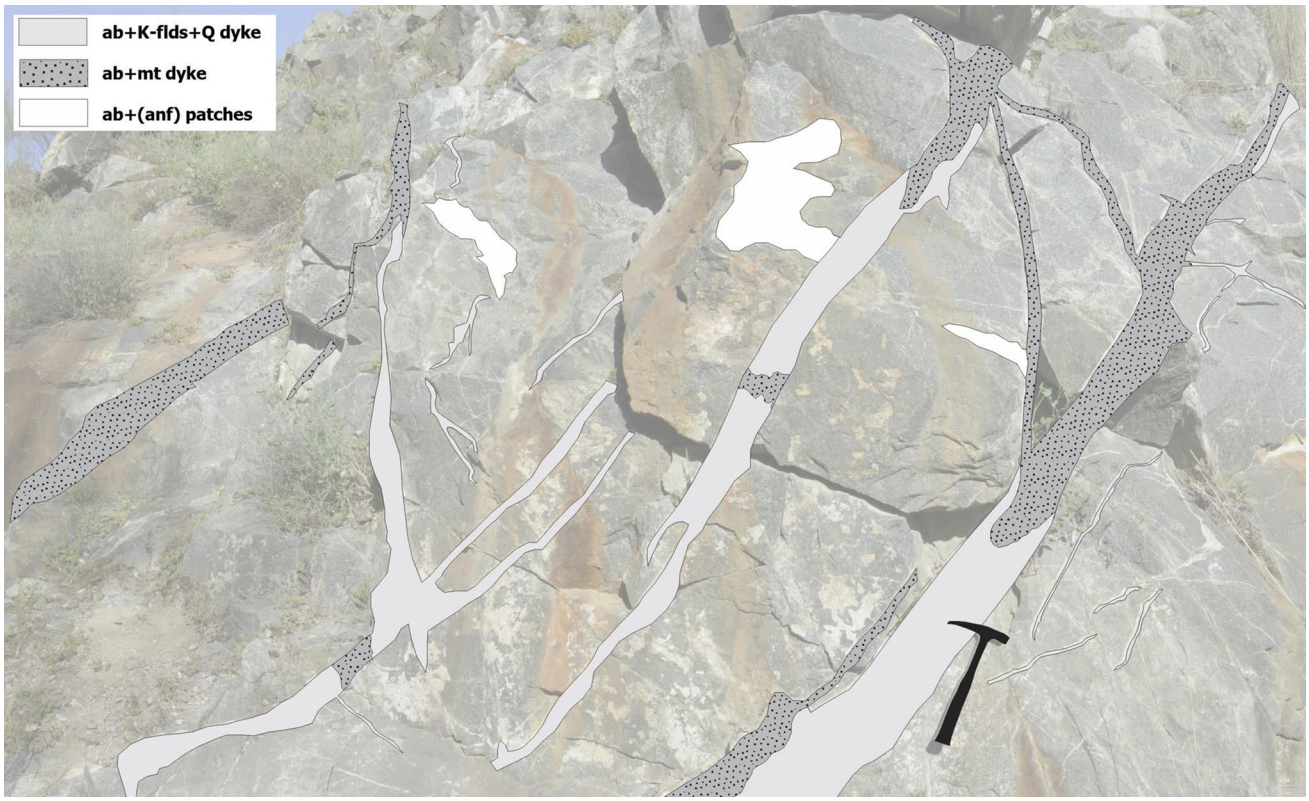

Fig. 6 Detailed mapping and discrimination of an albite rich dyke system Colmenar, better preserved by an undefformed gabbro within the open pit close to the main orebody footwall. Albite rich ocurrences have been discriminated based on dominant mineralogy within the dykes and irregular patches

7 Mineralization and hydrothermal alteration

The main known orebody at Colmenar has an elongated shape along a N35–45° E trend dipping 75° W, with a surface exposure of about 500 m and an average thickness of 30 m. This stratabound mineralization is slightly discordant with the N20° E bedding distribution. Its morphology seems to be controlled by the Colmenar Shear Band (Fig. 3) and the presence of the carbonatic and calc-silicate rocks of the Las Mayorgas Formation.

The ore-bearing sequence show high degrees of hydrothermal alteration along inner parts within the sheared zone. Mineralized rocks there are formed by a coarse-grained aggregate of magnetite albite and ferroactinolite with zones of massive magnetite. In the outermost areas surrounding the sheared corridor, mineralization occurs as jigsaw type breccias and veining, with a hydrothermal assemblage of ferroactinolite-magnetite, sometimes with pink calcite, pyrite, quartz and chlorite (Fig. 8a).

Petrographically, mineralized rocks show mosaic equigranular textures with actinolite-ferroactinolite and albite (an < 10), accompanied by variable proportions of magnetite (Fig. 8b, c). Magnetite shows various morphologies, from euhedral to anhedral grains, suggesting polyphasic growth with possible later remobilization and recrystallization Some anhedral cores could represent inherited sedimentary magnetite. Accessory minerals are quartz, scapolite, titanite, pyrite, hedenbergite, ilvaite, epidote, apatite, monazite, xenotime and, very occasionally, euhedral zircon, the latter interpreted to be inherited from an igneous protolith by Sanabria et al. (2005). There are also remnants of magnesio-hornblende that are interpreted as inherited from an amphibolitic protolith.

The eastern tonalite is replaced by albite and the mafic minerals by ferroactinolite; the clinoamphibole is gradually replaced by magnetite. This Na-Fe-rich metasomatism increases towards the contact with the sheared mineralized zone. Small isolated bodies of a garnet-rich skarn at the contact between the calc-silicate rocks and the eastern tonalite. This calcic skarn consists of large crystals of andradite that are replaced by epidote and quartz, without any signs of deformation.

The main mineralization shows a characteristic compositional banding marked by different proportions of albite vs actinolite with magnetite. Relicts of the calc-silicate rocks up to the metric scale float in a ferroactinolite-albite-magnetite groundmass, generally rotated and gradually replaced till its complete

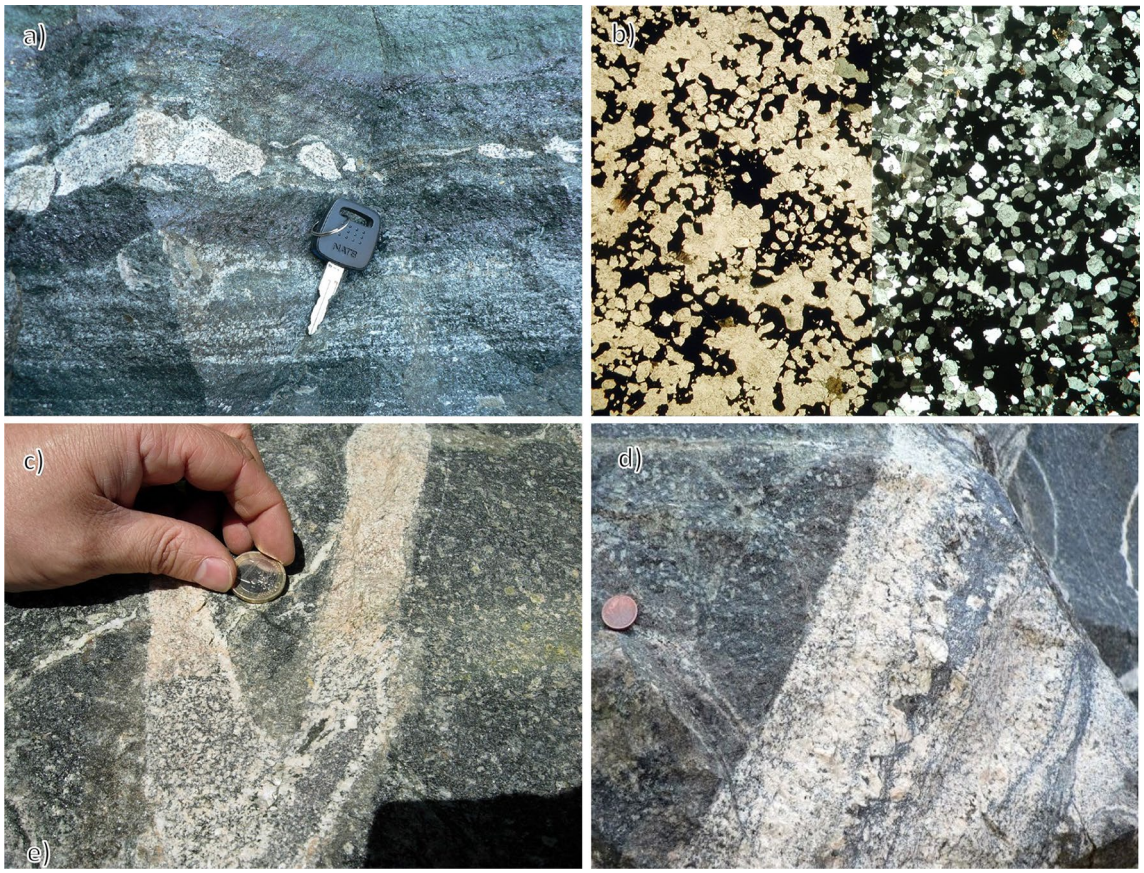

Fig. 7 **a** Whitish albite magnetite dykes within the main orebody at Colmenar, showing an irregular and discontinuous distribution following a preferent orientation along foliation and shearing associated with Colmenar shear band and the orebody. Boudinated shapes and lobulated contacts suggest a general magmatism synchronous with deformation, even if punctually fractured examples under more brittle conditions have been observed. Lobulated contacts are also responding to intense hydrothermal activity associated and development of metasomatic fronts, with variable degrees of replacement of the host rocks by an association of actinolite and magnetite; **b** detail of of albite-magnetite rich dykes internal holocrystalline texture, dominated by albite and actinolite equilibrium textures with homogeneous grain size, with minor contents of amphibole, titanite and zircon (left not analyzed light, right analyzed light, 3.2×); **c** detail within an albitic dyke of two different mineral assemblages, a whitish one at the top dominated by albite, and a more heterogenous one with coexisting albite and magnetite. The sharp contact transition within the same structure and without clear evidences of reaction borders or hydrothermal alteration point to discrete magma immiscibility process as the most likely explanation; **d** Albite–Magnetite rich dyke showing heterometric albite crystals with unidirectional growth textures (UST), with crystallization perpendicular to dyke margins and internal magmatic banding

obliteration. Preserved relicts of other recrystallized rocks from the Mayorgas Fm are occasionally found, showing only a local replacement of wollastonite and diopside. As described above, the mineralization includes abundant dykes of albite-magnetite, subparallel to the compositional banding (Fig. 7a).

Various kinematic evidences of ductile–brittle shearing can be identified along the shear zone and mineralization. Abundant boudinated forms indicate stretching processes under rheologic contrasts. Features such as rotation, and dismemberment are frequent in the relicts of the hosting rocks (Fig. 8d). Tension cracks developed perpendicular to the general compositional banding are frequent and suggest a dominant sinistral component and are frequently filled by sulfides (Fig. 8e).

The banded textures at Colmenar mineralization could be partially inherited from the fine-grained compositional layering at the calc silicate hornfels. However, the dominant trend oblique to the sedimentary layering (Fig. 8f), the coarse-grained assemblages and the kinematic evidences of ductile–brittle shearing suggest a ultimate tectonic-hydrothermal origin for the banding.

At Colmenar, the sulfide content is low, dominated by pyrite with sub-economic concentrations of chalcopyrite and traces of pyrrhotite, millerite and bornite with some gold. Pyrite crystallizes as euhedral crystals, generally late in the mineral assemblage formation, enclosing magnetite or intergrown with clinoamphibole. Usually sulfides are more

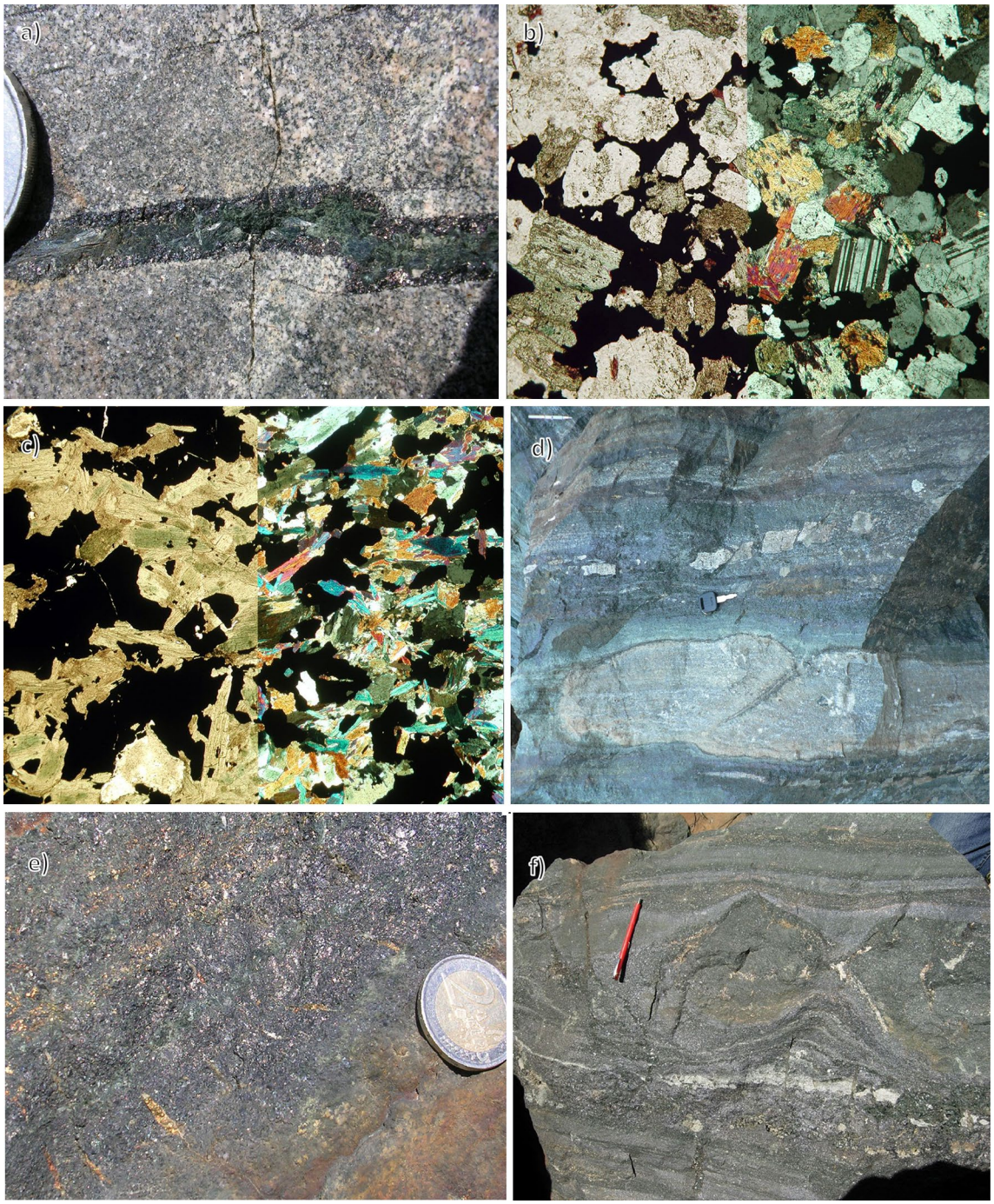

Fig. 8 **a** Iron mineralization at Colmenar with a paragenesis dominated by albite, actinolite and magnetite holocrystalline textures with accessory titanite, apatite and rutile (left no analyzed light, right analyzed light, 10×); **b** high grade iron mineralization at Colmenar, slightly enriched in sulphides, and dominated by a well-developed holocrystalline texture with intergrown magnetite and ferroactinolite crystals up to over 1 cm (left not analyzed light, right analyzed light, 3.2×); **c** hydrothermal vein at Colmenar surroundings with development of an external zone of magnetite crystals at contact with the host rock, and infilled by an association of actinolite with traces of sulphides; **d** compositional banding observed at Colmenar main orebody, subparallel to the shearing with examples of boudinated textures abundant on unaltered protolith relicts; **e** Marble and albite-magnetite relicts within the main orebody at Colmenar, the later showing locally a more brittle fracturing and displacement. The marble relict shows corroded borders affected by hydrothermal alteration; **f** detail of tension gashes infilled by sulphides (pyrite) developed subperpendicular to the shearing banding at Colmenar main orebody

abundant in the high-grade magnetite zones, with a higher degree of replacement.

8 Relationship between the albitite and the hydrothermal mineralization

The northern sector of the open pit shows the relationships between the different types of albitite and the hydrothermal alteration related to the mineralization. Figure 9a shows outcropping transition examples between albitic breccias and dykes. The albite supported breccias show a gradual transition to discrete clast-supported breccias with related pervasive alteration. Albite proportion decreases at this breccias and ends dominated by magnetite-ferroactinolite with only minor contents of titanite and calcite.

Titanite is particularly common when the albitic breccia is hosted by the gabbro-amphibolite host rocks. Titanite crystals up to > 2 mm in size crystallized in equilibrium with albite, punctually coexisting with well-developed intergrowth ferroactinolite (Fig. 9b). Ferroactinolite is dominant in all hydrothermally altered rocks at Colmenar, suggesting its formation close to the magmatic-hydrothermal transition (Fig. 9b).

Outcrops in the north-west sector of the deposit show large zones of hydrothermal breccias with a jigsaw pattern and cm-sized angular clasts of tonalite supported by magnetite and actinolite with local interstitial calcite (Fig. 9c). These relationships suggest that at least part of the hydrothermal alteration and mineralization would be subsequent to the intrusion and crystallization of the tonalitic Brovales Pluton.

9 Methodology and material

An isotopic study was carried out since discrepancies exist in literature regarding the ages of these unusual albite-rich rocks, spatially associated with iron mineralization in the Ossa Morena Zone. Most intrusions are attributed to the Cambrian as emplaced during the rift processes (Sánchez-García et al. 2008), something that contradicts the Variscan ages of the metamorphism in the Valuengo area (Apraiz and Eguiluz 2002).

A Variscan age for metamorphism and migmatization is consistent with our observations at Colmenar, where crosscutting relationships indicate that at least some of the mineralization and albitite postdate the emplacement of the Brovales Pluton; this is also consistent with a Sm–Nd isochron obtained on a magnetite concentrate from the main mineralization at Colmenar, indicating an age of 334 ± 32 Ma (Darbyshire et al. 1998).

The sampling was focused on covering the main hydrothermal and magmatic processes identified at Colmenar.

For U–Pb dating, zircon concentrates were obtained from both the eastern tonalite (sample JCO67) and the albite-rich dykes (samples JCO43 and JCO66). We were unable to obtain zircon concentrates from the gabbro. U–Pb dating also includes coarse-grained titanite of the albite-rich breccias, (sample JCO75). Prior to isotopic analysis of concentrates, samples were characterized by petrography, electron microscopy and cathodoluminescence. The analytical techniques used were TIMS or SHRIMP, chose based on spatial resolution needs.

Ar–Ar dating was performed on two calcic clinoamphibole concentrates from the main stratabound orebody (JCO62 and JCO72). Ferroactinolite, as determined by EPMA, hosts amount of K for dating, probably substituting Ca, and form large euhedral crystals intergrown with albite and magnetite, interpreted as representative of the ore forming hydrothermal event.

Radiogenic isotopes are also used to trace the origin of fluids in the system. Two representative samples of the mineralization (JCO44 and JCO45), and one of the garnet-rich skarn (JCO46) have been analyzed for Sr and Nd isotopes. Likewise, two samples were taken from the albite-magnetite dikes (JCO43 and JCO66), and one from the plagioclase-rich groundmass from the magmatic breccias (JCO47). Finally, two gabbro samples (JCO4 and JCO5) and two samples of the eastern tonalite (JCO1 and JCO7) were collected. The Rb–Sr and Sm–Nd results obtained on whole rock samples of Colmenar are reported in Table 4. The εNd parameter has been calculated using the age of 340 Ma for all lithologies, an age assumed to the representative of the mineralization and related Variscan magmatism.

U–Pb TIMS*:* This method was performed at the Earth Science Department from Geneva's University (Switzerland). Zircon crystals were subjected to an annealing process for internal structure homogenization during 48 h at a temperature of 900 °C. Chemical abrasion, zircon dissolution and later chromatography as well as with a Thermo Finnigan mass spectrometer where performed following the method referred on (Chiaradia et al. 2009).

U–Pb SHRIMP*:* Isotopic determinations were performed by the SHRIMP-II at the Geological Survey of Canada (Otawa). SHRIMP analytical procedures followed those described by Stern (1997), with standards and U–Pb calibration methods following Stern and Amelin (2003). Briefly, a selection of a hundred zircon grains from the sample JCA60 (see zircon petrography description), were cast in 2.5 cm diameter epoxy mounts (GSC #473) along with fragments of the GSC laboratory standard zircon (z6266, with $^{206}Pb/^{238}U$ age = 559 Ma). The mid-sections of the zircons were exposed using 9, 6, and 1 µm diamond compound, and the internal features of the zircons (such as zoning, structures,

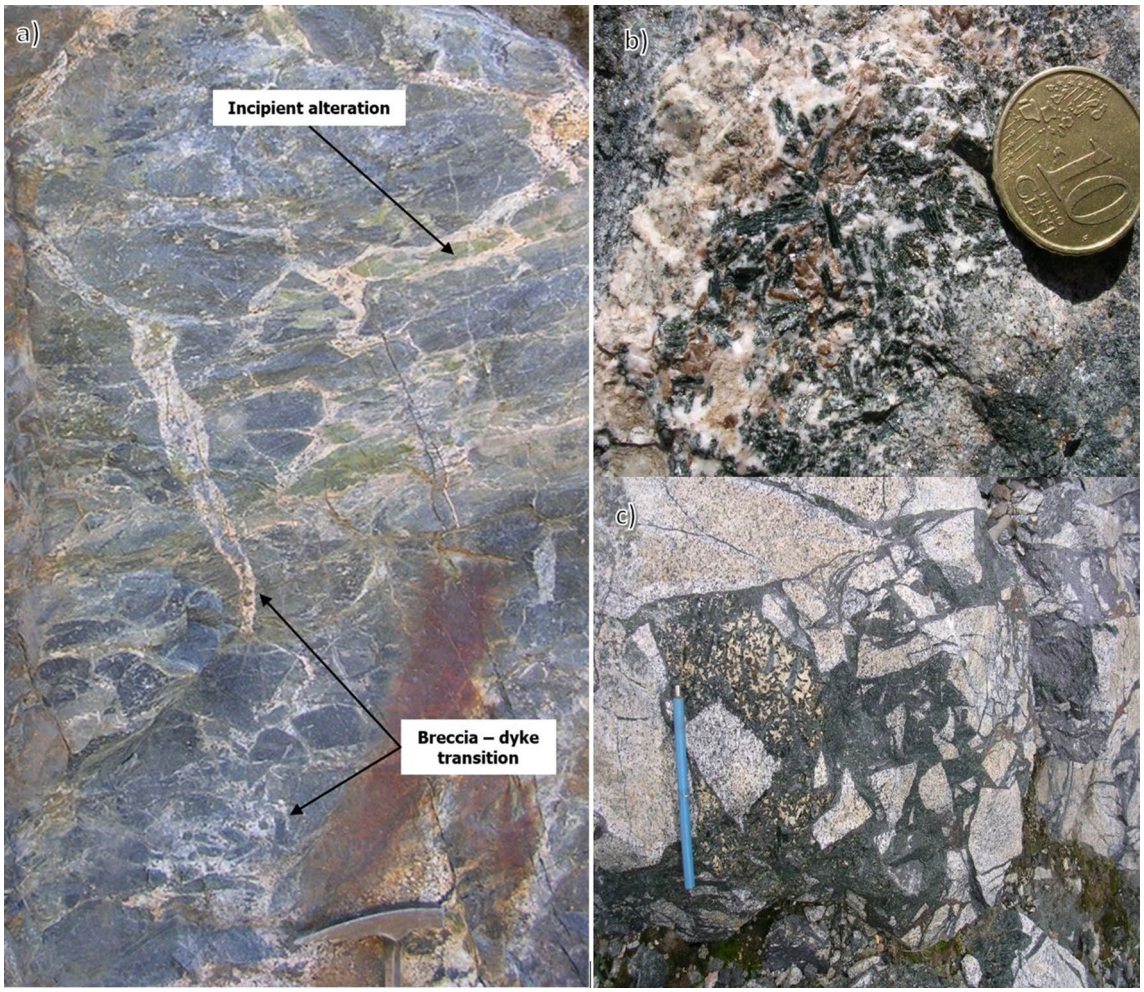

Fig. 9 **a** Outcropping gabbro at NE sector of Colmenar open pit in close contact with the main orebody. Can be clearly observed an evolution of whitish albitic rocks from magmatic breccia zones migrating through dyke type intrusions with relevant amounts of magnetite. At this outcrop can be observed an incipient to intermediate calcic alteration on epidotized clasts, just few meters away from the Colmenar main orebody; **b** Detail of an albitic dyke contact with development of centimetric euhedral brownish Titanite crystals intergrown with centimetric greenish ferroactinolite, albite and magnetite, main mineralization assemblage at Colmenar deposit. The clear equilibrium between titanites commonly observed at albitic rocks, and ferroactinolites, as the main hydrothermal mineral accompanying iron mineralization, evidences a magmatic/hidrotermal transition process; **c** Granodiorite from Brovales Pluton at the upper west benches of Colmenar open pit. A spectacular hydrothermal brecciation, with heterometric angular granodiorite clasts supporte by a magnetite-actinolite matrix, with punctual vugs infilled by calcite and minor sulphides. This outcrop demonstrates that at least part of the iron mineralization at Colmenar is younger than Brovales intrusion

alteration, etc.) were characterized in cathodoluminescence mode (CL) in order to select the samples and points to be analyzed. Mount surfaces were evaporatively coated with 10 nm of high purity Au. Analyses were conducted using a 16O- primary beam, projected onto the zircons at 10 kV. The sputtered area used for analysis was ca. 16 µm in diameter with a beam current of ca. 4 nA. The count rates of ten isotopes of Zr+, U+, Th+, and Pb+ in zircon were sequentially measured over 6 scans with a single electron multiplier and a pulse counting system with deadtime of 23 ns. Off-line data processing was accomplished using customized in-house software. The 1σ external errors of $^{206}Pb/^{238}U$ ratios reported in the data table incorporate a ± 1.4% error in calibrating the standard zircon (Stern and Amelin 2003). No fractionation correction was applied to the Pb-isotope data; common Pb correction utilized the measured $^{207}Pb/^{206}Pb$ and compositions of the surface blank (Stern 1997).

Ar–Ar: *S*amples were analyzed by the $^{40}Ar/^{39}Ar$ method at the University of Nevada at Las Vegas, were wrapped in Al foil and stacked in 6 mm inside diameter sealed fused

silica tubes. Individual packets averaged 3 mm thick and neutron fluence monitors (FC-2, Fish Canyon Tuff sanidine) were placed every 5–10 mm along the tube. Synthetic K-glass and optical grade CaF_2 were included in the irradiation packages to monitor neutron induced argon interferences from K and Ca. Loaded tubes were packed in an Al container for irradiation. Samples irradiated at the U. S. Geological Survey TRIGA Reactor, Denver, CO were in-core for 7 h in the In-Core Irradiation Tube (ICIT) of the 1 MW TRIGA type reactor. Correction factors for interfering neutron reactions on K and Ca were determined by repeated analysis of K-glass and CaF_2 fragments. Measured ($^{40}Ar/^{39}Ar$) K values were 1.50 (±48.76%) × 10–2. Ca correction factors were ($^{36}Ar/^{37}Ar$) Ca = 2.72 (± 1.92%) × 10–4 and ($^{39}Ar/^{37}Ar$) Ca = 6.91 (± 1.80%) × 10–4. J factors were determined by fusion of 4–8 individual crystals of neutron fluence monitors which gave reproducibility's of 0.11% to 0.52 at each standard position. Variation in neutron fluence along the 100 mm length of the irradiation tubes was < 4%. Matlab curve fit was used to determine J and uncertainty in J at each standard position. No significant neutron fluence gradients were present within individual packets of crystals as indicated by the excellent reproducibility of the single crystal fluence monitor fusions.

Irradiated FC-2 sanidine standards together with CaF_2 and K-glass fragments were placed in a Cu sample tray in a high vacuum extraction line and were fused using a 20 W CO2 laser. Sample viewing during laser fusion was by a video camera system and positioning was via a motorized sample stage. Samples analyzed by the furnace step heating method utilized a double vacuum resistance furnace similar to the (Staudacher et al. 1978) design. Reactive gases were removed by three GP-50 SAES getters prior to being admitted to a MAP 215-50 mass spectrometer by expansion. The relative volumes of the extraction line and mass spectrometer allow 80% of the gas to be admitted to the mass spectrometer for laser fusion analyses and 76% for furnace heating analyses. Peak intensities were measured using a Balzers electron multiplier by peak hopping through 7 cycles; initial peak heights were determined by linear regression to the time of gas admission. Mass spectrometer discrimination and sensitivity was monitored by repeated analysis of atmospheric argon aliquots from an on-line pipette system. Measured $^{40}Ar/^{36}Ar$ ratios were 281.06 ± 0.35% during this work, thus a discrimination correction of 1.0514 (4 AMU) was applied to measured isotope ratios. The sensitivity of the mass spectrometer was ~ 6 × 10–17 mol mV-1 with the multiplier operated at a gain of 36 over the Faraday. Line blanks averaged 4.20 mV for mass 40 and 0.02 mV for mass 36 for laser fusion analyses and 7.05 mV for mass 40 and 0.03 mV for mass 36 for furnace heating analyses. Discrimination, sensitivity, and blanks were relatively constant over the period of data collection. Computer automated operation of the sample stage, laser, extraction line and mass spectrometer as well as final data reduction and age calculations were done using LabSPEC software written by B. Idleman (Lehigh University). An age of 28.02 Ma (Renne et al. 1998) was used for the Fish Canyon Tuff sanidine fluence monitor in calculating ages for samples.

For $^{40}Ar/^{39}Ar$ analyses a plateau segment consists of 3 or more contiguous gas fractions having analytically indistinguishable ages (i.e. all plateau steps overlap in age at ± 2σ analytical error) and comprising a significant portion of the total gas released (typically > 50%). Total gas (integrated) ages are calculated by weighting by the amount of ^{39}Ar released, whereas plateau ages are weighted by the inverse of the variance. For each sample inverse isochron diagrams are examined to check for the effects of excess argon. Reliable isochrons are based on the MSWD criteria of (Wendt and Carl 1991) and, as for plateaus, must comprise contiguous steps and a significant fraction of the total gas released. All analytical data are reported at the confidence level of 1σ (standard deviation).

Rb–Sr & Sm–Nd: The samples were milled to analytical powder size at the IGME sample preparation labs (Madrid, Spain). Whole rock were first decomposed in 4 ml HF and 2 ml HNO_3, in Teflon digestion bombs during 48 h at 120 °C and finally in 6 M HCl. Concentrations of Rb and Sr as well as Rb/Sr atomic ratios were determined by X-ray fluorescence spectrometry at the X-Ray Diffraction Centre of the Complutense University following the methods of (Pankhurst and O´nions 1973*). Sm and Nd were determined by isotope dilution using spikes enriched in ^{149}Sm and ^{150}Nd. Ion exchange techniques were used to separate the elements for isotopic analysis. Sr and REE were separated using Bio-Rad AG50 × 12 cation exchange resin. Sm and Nd were further separated from the REE group using Bio-beads coated with 10% HDEHP. The Rb–Sr and Sm–Nd isotope composition were determined on an automated multicollector SECTOR 54® mass spectrometer at the Geochronology and Isotope Geochemistry Centre of the Madrid University.

Errors are quoted throughout as two standard deviations from measured or calculated values. The decay constants used in the calculations are the values $\lambda^{87}Rb = 1.42 \times 10–11$ and $\lambda^{147}Sm = 6.54 \times 10–12$ year-1 recommended by the IUGS Subcommission for Geochronology (Steiger and Jäger 1997). Analytical uncertainties are estimated to be 0.01% for $^{87}Sr/^{86}Sr$ ratios and 0.006% for $^{143}Nd/^{144}Nd$ ratios and 1.0% and 0.1% for the $^{87}Rb/^{86}Sr$ and $^{147}Sm/^{144}Nd$ ratios, respectively. Epsilon-Nd (εNd) values (Jacobsen and Wasserburg 1980) were calculated relative to a chondrite present-day $^{143}Nd/^{144}Nd$ value of 0.51262 and $^{147}Sm/^{144}Nd$ of 0.1967. Replicate analyses of the NBS-987 Sr-isotope standard yielded an average $^{87}Sr/^{86}Sr$ ratio of 0.710247 ± 0.000024 ($n = 215$). Fifty-six analyses of the Johnson Matthey

Nd-standard over 1 year gave a mean $^{143}Nd/^{144}Nd$ ratio of 0.511114 ± 0.000026.

10 Geochronology and isotope geochemistry

10.1 U–Pb dating

The tonalite has two zircon morphological populations (P1 and P2). P1 includes euhedral zircon grains, with elongated prismatic habits and poor development of bipyramidal terminations. Its average size for its long axis is around 500 µm. Zircon grains have a transparent glassy appearance, without evidence of solid inclusions. Cathodoluminescence imaging reveals a single concentric zoning in all of them, suggesting that the zircons were formed during a single magmatic crystallization event (Fig. 10a). This banding is quite common in magmatic zircons and interpreted as due to compositional variations in U, Th and REE (Corfu et al. 2003).

P2 zircons present similar color and transparency but their general shapes, are not so elongated, and may even become sub-rounded. They are smaller in size with respect to P1, not exceeding 300 µm on their longest axis. Bipyramidal ends are better developed than in P1, being able to conform up to two thirds of the crystal. The cathodoluminescence images do not show evidences of inherited cores and present the characteristic zoning of single stage growth (Fig. 10a).

Both populations are similar to the G1 and G2 types of Pupin (1980), and based on this, both identified morphologies can coexist in magmas with a high Al/(Na + K) ratio, and under crystallization conditions around 600 °C. However, given the subjectivity of this classification technique, this approach must be taken with caution. Additional factors influence zircon morphology (Belousova 2006), such as magma chemistry, water content or cooling speed. Both populations were analyzed by TIMS independently to contrast results and confirm or discard a single crystallization event over 4 zircons from P1 and 3 zircons from P2.

The zircon grains concentrated from the albitic dykes rarely exceed 150 microns in size and present frequent opaque inclusions. The degree of crystallinity is relatively low, showing heterogeneous habits, accompanied by broken, truncated and sometimes sub-rounded morphologies. It has not been possible to clearly discriminate specific zircon populations, with a predominant habit pointing to elongated bi-pyramidal morphologies.

Cathodoluminescence imaging highlights textural complexities. The presence of one or up to two subsequent stages of crystalline growth can be identified, with different degrees of development around the zircon cores, varying from 50 to 5–10 µm thick, more developed on zircon terminations (Fig. 10b). Corroded borders are punctually observed at the interface between two different zonings, clearly discriminating different crystallization stages. Based on these observations, a complex evolution of these zircons is highlighted, characterized by inherited cores with rounded morphologies typical of detrital zircons.

In order to obtain a representative age of these albite magmas, it was necessary to use a dating technique with high spatial resolution (SHRIMP), capable of analyzing the zircon rims, which represent the last crystallization event. Treatment of sample JCO43 has yielded only a small amount of zircon grains with abundant imperfections making it the least suitable sample for dating. Even so, a total of 15 determinations using SHRIMP have been carried out on various crystals, including some on inherited cores. Sample JCO66 was found to be richer in zircon grains and less fractured, with a total of 37 measurements performed.

The petrographic study of the titanite grains shows the predominance of euhedral forms reflecting crystallization in equilibrium with the rest of the rock. In turn, the study by backscattered electron microscopy (BSE) shows that the crystals are homogeneous and lack evidences of internal zoning or heterogeneities that could be indicative of polyphasic growth. Its homogeneity makes them suitable for dating by TIMS, that was performed on 3 selected crystals.

The results obtained by TIMS for the zircon and titanite grains are reported in Table 1. The results obtained by SHRIMP for zircons of samples JCO46 and JCO66, are reported in Tables 2 and 3 respectively.

The results from the eastern tonalite (JCO67) do not allow us to establish a concordant age for all zircon grains in population 1, but excluding one sample, a concordia age of 338.26 ± 0.32 Ma is obtained (MSWD = 0.88). Regarding population 2, the three zircon grains yield a concordia age of 338.56 ± 0.33 Ma (MSWD = 3.9). Both ages overlap within uncertainty and therefore a similar crystallization age is assumed for both populations.

Pooling together the two populations, a concordia age of 338.42 ± 0.31 Ma (Fig. 11) is obtained for the eastern foliated tonalite (MSWD = 2.3), as an accurate age for Brovales plutonism.

From the results obtained by SHRIMP for the albite dykes, it was observed that sample JCO43 presents a more discordant character with respect to sample JCO66. This is probably due to Pb loss, consistent with the more heterogeneous and fractured appearance of the zircons as described above. Taking this fact into account, the main interpretation of results is focused on sample JCO66, using JCO43 as a comparative reference.

One analysis from sample JCO66 showed an extremely old age of 2564.3 ± 48.5 Ma (Table 3), close to the Archean—Proterozoic boundary, while 7 results pointed to ages between the Paleoproterozoic (2.07 ± 48 Ga) and the base of the Edicarian. All these ages are outside the range

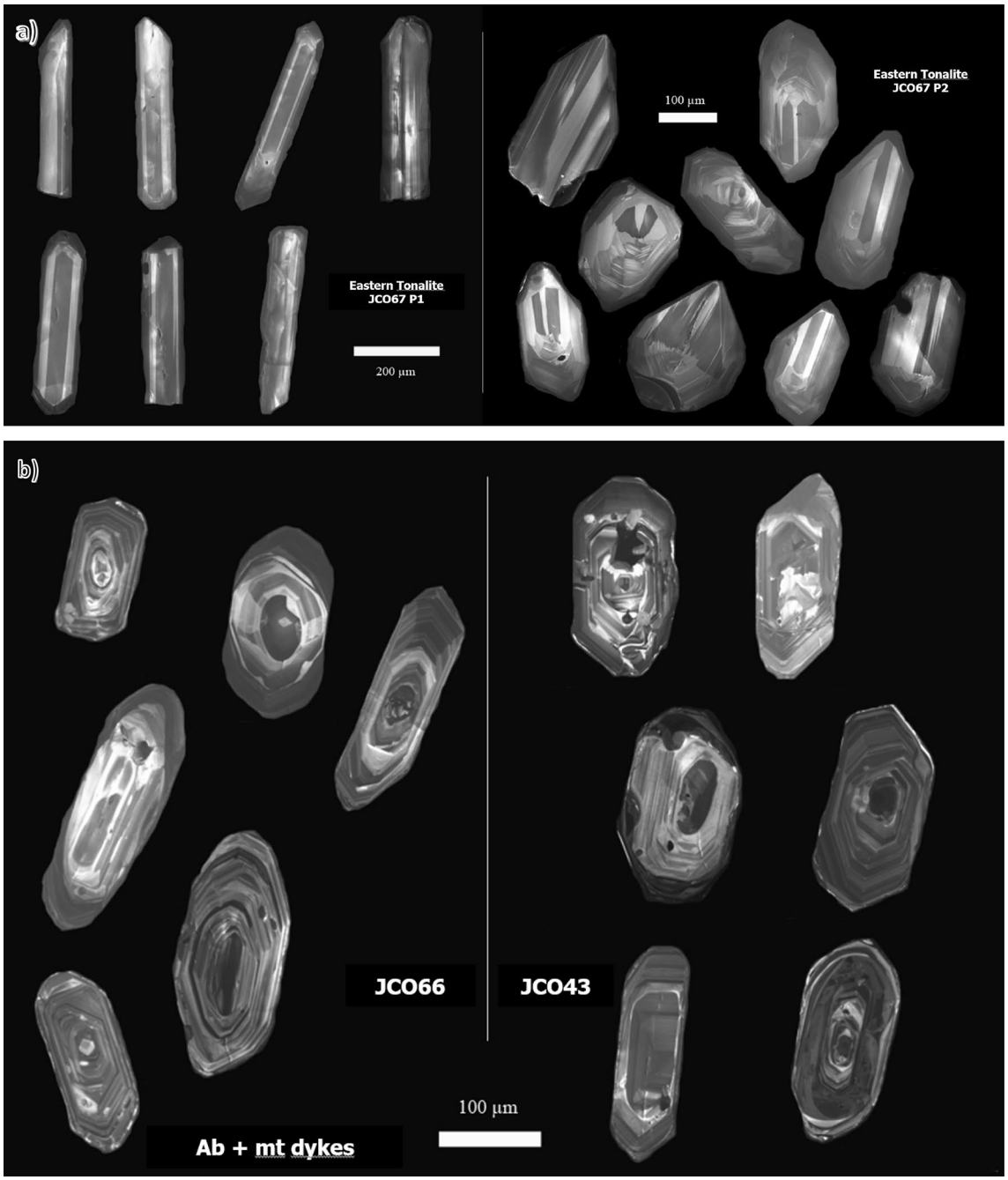

Fig. 10 **a** Cathodoluminescence imaging and morphological comparison of the two zircon populations discriminated from the eastern Tonalite concentrate (JCO67); **b** Cathodoluminiscence imaging from samples corresponding to the albite-magnetite dykes (JCO43, JCO66).

of stratigraphic ages identified in the Ossa Morena area, and likely represent detrital zircons from an older basement.

Younger ages obtained from both samples have been plotted in a histogram (Fig. 12), where it can be observed that the age spectrum ranges is characterized by two well-defined geological events, from the upper Neoproterozoic (Edicarian) to Middle Carboniferous, with a minimum age of 326.7 ± 4.6 Ma.

The most abundant range of ages obtained ranges between 660 and 520 Ma, with a peak between 580 and 560 Ma (Upper Proterozoic). These ages were obtained by analyzing both inherited cores and most external halos, as well as in some specimens that apparently have a single stage growth. This age range would be correlated with the Neoproterozoic stratigraphic sequence of the Ossa Morena Zone (Serie Negra), dated at 591 ± 11 Ma (Ordóñez 1998), and within which the Las Mayorgas Formation is included. This ages also present high correlation with the detrital zircon ages of the Ossa Morena Basement (Pereira et al. 2011). Our best

Table 1 U/Pb TIMS isotopic ratios obtained at Colmenar for the two zircon populations (P1 y P2) from the Eastern tonalite and titanite from the albitic dykes

No	Weight (mg)	Concentration		Pb com pg	Th/U[a]	Atomic ratios								Ages		Coef Corr (rho)	disc. %
		U (ppm)	Pb (ppm)			$^{206}Pb/^{204}Pb^{b}$	$^{207}Pb/^{206}Pb^{b,c,d}$	Error 2σ (%)	$^{207}Pb/^{235}U^{b,c}$	Error 2σ (%)	$^{206}Pb/^{238}U^{d}$	Error 2σ (%)	206/238	207/235	207/206		
JCO67P1 (zircon)																	
1	0.0105	248.349	13.39	0.000	0.35	1676.696	0.053274	0.15	0.39615	0.16	0.05393	0.05	338.6	338.7	339.1	0.37	0.15
2	0.0083	185.627	10.024	0.000	0.35	4395.507	0.053304	0.18	0.39583	0.19	0.05386	0.05	338.2	338.6	341.8	0.31	1.05
3	0.0088	221.287	11.859	0.000	0.33	2465.421	0.053261	0.16	0.39541	0.17	0.05384	0.05	338.1	338.3	339.9	0.32	0.53
4	0.0038	210.107	14.018	2.571	0.38	235.9620	0.053297	0.40	0.39597	0.43	0.05388	0.07	338.3	338.7	341.4	0.47	0.91
JCO67P2 (zircon)																	
1	0.0055	189.388	10.903	0.740	0.33	783.3581	0.053365	0.14	0.39648	0.16	0.05389	0.05	338.3	339.1	344.3	0.44	1.74
2	0.0031	237.969	12.662	0.000	0.30	506.3992	0.053310	0.23	0.39605	0.25	0.05388	0.06	338.3	338.8	342.0	0.44	1.08
4	0.0044	314.591	22.693	5.949	0.30	196.7927	0.053327	0.28	0.39642	0.30	0.05391	0.07	338.5	339.1	342.7	0.42	1.23
JCO75 (titanite)																	
2	0.0055	109.925	12.978	2.144	3.44	190.9558	0.053092	0.49	0.39332	0.67	0.05373	0.43	337.4	336.8	332.7	0.69	-1.41
3	0.0031	146.196	14.605	2.453	2.23	219.8400	0.053683	0.78	0.39555	0.85	0.05344	0.22	335.6	338.4	357.8	0.46	6.20
4	0.0044	101.638	11.644	1.857	3.21	203.2828	0.053317	0.60	0.39353	0.66	0.05353	0.17	336.2	336.9	342.3	0.46	1.78

[a]Calculated on the basis of radiogenic $^{208}Pb/^{206}Pb$ ratios, assuming concordance

[b]Corrected from fractionation and spike

[c]Corrected for fractionation, spike, blank and common lead (according to Stacey and Kramers 1975)

[d]Corrected for initial ^{230}Th disequilibrium, assuming a Th/U = 4 in the source

Table 2 U/Pb isotopic ratios obtained by SHRIMP over zircons from sample JCO43, corresponding to the albite-magnetite dykes at Colmenar

Spot name	U (ppm)	Th (ppm)	Th/U	Pb^t (ppm)	Uncorrected ratios											Corrected ages (Ma)	
					$\frac{^{204}Pb}{^{206}Pb}$	$\pm\frac{^{204}Pb}{^{206}Pb}$	$\frac{^{208}Pb}{^{206}Pb}$	$\pm\frac{^{208}Pb}{^{206}Pb}$	$\frac{^{207}Pb}{^{235}U}$	$\pm\frac{^{207}Pb}{^{235}U}$	$\frac{^{206}Pb}{^{238}U}$	$\pm\frac{^{206}Pb}{^{238}U}$	Corr coeff	$\frac{^{207}Pb}{^{206}Pb}$	$\pm\frac{^{207}Pb}{^{206}Pb}$	$\frac{^{206}Pb}{^{238}U}$	$\pm\frac{^{206}Pb}{^{238}U}$
JCO43-11.1	1538	245	0.16	88	2.54E-03	1.26E-04	0.1271	0.0042	0.677	0.013	0.0544	0.0008	0.8089	0.0903	0.0010	326.7	4.6
JCO43-12.1	859	131	0.16	45	6.26E-04	9.89E-05	0.0527	0.0028	0.443	0.011	0.0548	0.0009	0.7407	0.0587	0.0009	341.5	5.2
JCO43-4.1	793	85	0.11	52	3.32E-04	6.11E-05	0.0384	0.0021	0.573	0.013	0.0690	0.0010	0.7380	0.0602	0.0009	427.7	6.1
JCO43-15.1	1255	35	0.03	95	1.01E-03	6.40E-05	0.0337	0.0017	0.795	0.014	0.0794	0.0012	0.9009	0.0726	0.0006	483.8	7.0
JCO43-7.1	1034	701	0.7	103	1.43E-03	1.56E-04	0.2220	0.0043	0.948	0.020	0.0891	0.0015	0.8611	0.0771	0.0008	538.4	8.8
JCO43-2.1	330	225	0.7	33	1.40E-03	1.49E-04	0.2311	0.0072	0.950	0.021	0.0899	0.0013	0.7632	0.0767	0.0011	543.0	7.9
JCO43-10.1	354	179	0.52	33	1.01E-04	1.10E-04	0.1430	0.0126	0.728	0.031	0.0893	0.0016	0.5192	0.0591	0.0022	551.3	9.5
JCO43-1.1	385	286	0.77	39	4.49E-04	1.02E-04	0.2226	0.0076	0.797	0.020	0.0906	0.0015	0.7461	0.0638	0.0011	555.9	8.8
JCO43-17.1	988	601	0.63	98	6.92E-04	6.83E-05	0.1821	0.0038	0.892	0.018	0.0924	0.0015	0.8609	0.0701	0.0007	562.1	9.0
JCO43-13.1	1508	127	0.09	134	1.20E-04	3.07E-05	0.0213	0.0016	0.786	0.015	0.0953	0.0014	0.8442	0.0598	0.0006	586.8	8.3
JCO43-9.1	732	178	0.25	67	2.47E-05	2.01E-05	0.0563	0.0026	0.780	0.015	0.0959	0.0014	0.8316	0.0590	0.0006	590.9	8.3
JCO43-6.1	143	194	1.4	17	8.09E-05	1.77E-04	0.3595	0.0149	0.826	0.029	0.0967	0.0020	0.6922	0.0620	0.0016	593.3	12.1
JCO43-16.1	435	611	1.45	58	1.05E-04	6.12E-05	0.4136	0.0095	0.922	0.019	0.1047	0.0015	0.7960	0.0639	0.0008	639.9	9.2
JCO43-8.1	528	631	1.23	70	3.44E-05	4.17E-05	0.3649	0.0134	0.915	0.025	0.1083	0.0018	0.6842	0.0613	0.0012	662.8	10.5
JCO43-14.1	363	451	1.28	236	1.43E-05	1.50E-05	0.3372	0.0056	12.504	0.215	0.4967	0.0080	0.9667	0.1826	0.0008	2564.3	48.5

Notes (see Stern, 1997): Spot name follows the convention x–y. z; where x = sample number, y = grain number and z = spot number. Uncertainties reported at 1 s (absolute) and are calculated by numerical propagation of all known sources of error Common Pb composition used for age correction is 0.895 ± 0.002, GSC surface common Pb (Stern 1997)

Pb^t = total Pb, uncorrected for common Pb

Calibration standard 6266; U = 910 ppm; Age = 559 Ma; $^{206}Pb/^{238}U = 0.09059$

Error in $^{206}Pb/^{238}U$ calibration 1.4%

Th/U calibration: F = 0.03900*UO + 0.85600

Table 3 U/Pb isotopic ratios obtained by SHRIMP over zircons from sample JCO66, corresponding to the albite-magnetite dykes at Colmenar

Spot name	U (ppm)	Th (ppm)	Th/U	Pb^t (ppm)	Uncorrected ratios											Corrected ages (Ma)	
					$\frac{^{204}Pb}{^{206}Pb}$	$\pm\frac{^{204}Pb}{^{206}Pb}$	$\frac{^{208}Pb}{^{206}Pb}$	$\pm\frac{^{208}Pb}{^{206}Pb}$	$\frac{^{207}Pb}{^{235}U}$	$\pm\frac{^{207}Pb}{^{235}U}$	$\frac{^{206}Pb}{^{238}U}$	$\pm\frac{^{206}Pb}{^{238}U}$	Corr coeff	$\frac{^{207}Pb}{^{206}Pb}$	$\pm\frac{^{207}Pb}{^{206}Pb}$	$\frac{^{206}Pb}{^{238}U}$	$\pm\frac{^{206}Pb}{^{238}U}$
JCO66-4.2	259	28	0.11	14	3.51E-03	5.83E-04	0.0517	0.0057	0.547	0.031	0.0543	0.0021	0.7609	0.0730	0.0027	333.2	12.5
JCO66-16.1	798	144	0.19	41	5.81E-05	5.16E-05	0.0543	0.0070	0.414	0.010	0.0541	0.0008	0.7070	0.0556	0.0010	338.7	5.1
JCO66-5.1	129	39	0.31	41	7 6.03E-05	4.56E-04	0.0924	0.0099	0.465	0.030	0.0546	0.0010	0.4103	0.0618	0.0036	339.0	6.5
JCO66-18.1	949	33	0.04	48	4.77E-05	4.13E-05	0.0098	0.0011	0.417	0.009	0.0551	0.0008	0.7524	0.0548	0.0008	345.2	5.1
JCO66-5.2	1491	276	0.19	78	7.35E-05	2.27E-05	0.051	0.0042	0.414	0.011	0.0554	0.0008	0.6643	0.0542	0.0011	347.0	5.1
JCO66-10.2	1526	32	0.02	78	2.19E-04	4.91E-05	0.0093	0.0010	0.426	0.008	0.0559	0.0008	0.8117	0.0553	0.0007	349.7	5.1
JCO66-24.1	805	586	0.75	72	2.13E-04	5.27E-05	0.2105	0.0104	0.704	0.014	0.0821	0.0012	0.8269	0.0622	0.0007	505.9	7.5
JCO66-3.1	154	4	0.03	12	1.00E-05	1.00E-05	0.0104	0.0032	0.715	0.030	0.0869	0.0014	0.4989	0.0597	0.0022	536.5	8.8
JCO66-2.1	170	44	0.27	15	5.87E-04	1.47E-04	0.0775	0.0063	0.846	0.028	0.0912	0.0016	0.6158	0.0672	0.0018	557.2	9.5
JCO66-7.2	1271	439	0.36	117	1.47E-04	4.78E-05	0.1082	0.0050	0.780	0.021	0.0912	0.0013	0.6333	0.0621	0.0013	560.4	8.1
JCO66-15.1	357	99	0.29	32	3.81E-05	5.09E-05	0.0732	0.0043	0.763	0.023	0.0922	0.0015	0.6323	0.0601	0.0014	567.8	9.1
JCO66-7.1	86	45	0.54	22	1.87E-02	1.10E-03	0.7688	0.0245	6.660	0.185	0.1409	0.0024	0.7080	0.3427	0.0068	574.0	11.9
JCO66-14.1	421	297	0.73	42	5.70E-05	5.42E-05	0.1852	0.0059	0.769	0.031	0.0934	0.0014	0.4721	0.0597	0.0022	575.4	8.3
JCO66-2.2	75	29	0.40	7	4.10E-04	2.70E-04	0.1091	0.0168	0.959	0.053	0.0957	0.0032	0.6993	0.0727	0.0029	579.9	18.9
JCO66-27.1	742	286	0.40	70	5.39E-05	2.59E-05	0.1047	0.0035	0.798	0.016	0.0946	0.0014	0.7886	0.0612	0.0008	581.2	8.3
JCO66-1.1	295	43	0.15	27	9.12E-05	7.82E-05	0.0402	0.0058	0.835	0.020	0.0959	0.0014	0.7140	0.0632	0.0011	587.7	8.6
JCO66-13.2	87	31	0.37	8	6.80E-04	4.23E-04	0.1055	0.0141	0.893	0.039	0.0966	0.0025	0.6932	0.0671	0.0021	589.1	15.0
JCO66-12.1	1181	333	0.29	111	2.30E-05	3.35E-05	0.0784	0.0056	0.789	0.014	0.0959	0.0014	0.8654	0.0596	0.0005	590.3	8.3
JCO66-17.1	948	60	0.07	85	5.51E-05	2.34E-05	0.0215	0.0017	0.802	0.015	0.0964	0.0014	0.8556	0.0603	0.0006	593.1	8.5
JCO66-22.1	1983	440	0.23	188	2.59E-04	2.65E-05	0.0683	0.0015	0.824	0.020	0.0974	0.0015	0.7163	0.0614	0.0010	598.2	8.8
JCO66-28.1	243	78	0.33	24	2.26E-04	8.86E-05	0.1036	0.0091	0.835	0.024	0.0982	0.0019	0.7472	0.0617	0.0012	602.7	11.3
JCO66-13.1	195	63	0.33	19	2.61E-04	9.60E-05	0.0917	0.0062	0.803	0.038	0.0981	0.0019	0.5117	0.0593	0.0024	603.9	11.2
JCO66-6.2	108	18	0.17	10	2.78E-04	3.91E-04	0.051	0.0062	0.951	0.033	0.1013	0.0018	0.5956	0.0681	0.0019	616.3	10.5
JCO66-8.2	790	57	0.07	74	2.65E-05	3.85E-05	0.019	0.0013	0.862	0.022	0.1006	0.0015	0.6687	0.0622	0.0012	616.5	8.9
JCO66-23.1	1766	654	0.38	178	5.88E-05	2.01E-05	0.1041	0.0044	0.836	0.034	0.1004	0.0030	0.8030	0.0604	0.0015	616.8	18.0
JCO66-20.1	1898	102	0.06	177	3.74E-04	3.80E-05	0.0153	0.0009	0.867	0.015	0.1008	0.0015	0.9070	0.0624	0.0004	617.9	8.6
JCO66-21.1	685	751	1.13	82	1.95E-05	3.71E-05	0.3197	0.0100	0.840	0.019	0.1011	0.0016	0.7759	0.0603	0.0009	621.0	9.3
JCO66-9.1	338	235	0.72	37	2.08E-04	7.38E-05	0.2011	0.0073	0.863	0.021	0.1020	0.0015	0.6949	0.0613	0.0011	625.7	9.2
JCO66-25.1	293	111	0.39	30	1.00E-05	1.00E-05	0.1061	0.0053	0.854	0.020	0.1026	0.0016	0.7328	0.0603	0.0010	630.0	9.4
JCO66-8.1	254	200	0.81	29	2.32E-04	1.52E-04	0.2211	0.0122	0.896	0.023	0.1044	0.0017	0.7112	0.0623	0.0011	639.0	9.9
JCO66-11.1	441	137	0.32	46	9.37E-05	5.93E-05	0.0961	0.0102	0.890	0.020	0.1045	0.0016	0.7610	0.0618	0.0009	640.0	9.6
JCO66-19.1	1476	12	0.01	146	2.37E-05	7.97E-06	0.0039	0.0005	0.969	0.018	0.1079	0.0015	0.8187	0.0651	0.0007	657.8	9.1
JCO66-10.1	189	57	0.31	21	2.65E-04	1.02E-04	0.0854	0.0113	1.038	0.029	0.1140	0.0020	0.7292	0.0660	0.0013	693.4	12.0
JCO66-26.1	874	585	0.69	115	1.23E-04	2.88E-05	0.2066	0.0082	1.068	0.020	0.1199	0.0018	0.8690	0.0646	0.0006	729.2	10.5
JCO66-11.2	70	67	0.98	13	4.08E-04	2.04E-04	0.2665	0.0168	1.683	0.057	0.1605	0.0034	0.7106	0.0760	0.0018	953.9	19.4

Table 3 (continued)

Spot name	U (ppm)	Th (ppm)	Th/U	Pb^{t} (ppm)	Uncorrected ratios										Corrected ages (Ma)	
					$\frac{^{204}Pb}{^{206}Pb}$	$\pm \frac{^{204}Pb}{^{206}Pb}$	$\frac{^{208}Pb}{^{206}Pb}$	$\pm \frac{^{208}Pb}{^{206}Pb}$	$\frac{^{207}Pb}{^{235}U}$	$\pm \frac{^{207}Pb}{^{235}U}$	$\frac{^{206}Pb}{^{238}U}$	$\pm \frac{^{206}Pb}{^{238}U}$	Corr coeff	$\frac{^{207}Pb}{^{206}Pb}$ $\pm \frac{^{207}Pb}{^{206}Pb}$	$\frac{^{206}Pb}{^{238}U}$	$\pm \frac{^{206}Pb}{^{238}U}$
JCO66-6.1	638	369	0.60	225	2.89E-05	1.66E-05	0.1512	0.0054	6.741	0.112	0.3144	0.0045	0.9174	0.1555 0.0010	1656.8	23.5
JCO66-4.1	133	124	0.96	60	1.58E-05	4.14E-05	0.2254	0.0056	7.469	0.152	0.3854	0.0062	0.8596	0.1406 0.0015	2072.3	34.7

Notes (see Stern, 1997): Spot name follows the convention x–y.z; where x = sample number, y = grain number and z = spot number. Uncertainties reported at 1 s (absolute) and are calculated by numerical propagation of all known sources of error Common Pb composition used for age correction is 0.895 ± 0.002, GSC surface common Pb (Stern 1997)

Pb$^{=}$ $^{=}$total Pb, uncorrected for common Pb

Calibration standard 6266; U = 910 ppm; Age = 559 Ma; $^{206}Pb/^{238}U = 0.09059$

Error in $^{206}Pb/^{238}U$ calibration 1.4%

Th/U calibration: F = 0.03900*UO + 0.85600

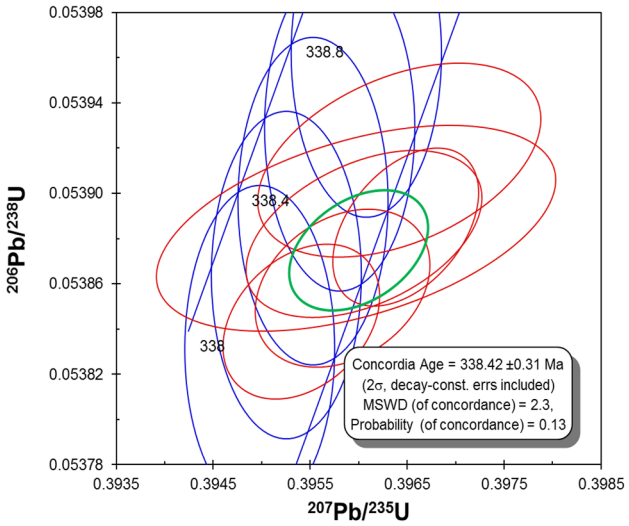

Fig. 11 Concordia age obtained from both populations of zircons from the eastern tonalite at Colmenar deposit

interpretation is that these ages are of the protolith from which the albitite derives by anatexis. These zircons, therefore, would be relicts embedded in the leucosome domains and physically transported in the magma during the injection of the dykes.

The younger age range, although less represented, shows a more constrained time range between 350 and 330 Ma (Fig. 12). These Variscan ages correspond to measurements taken on crystal rims, consistent with their systematic younger ages when compared with the above older ages. They represent the last crystallization event identified, corresponding to the crystallization age of the albitic dykes at 344.0 ± 4.6 Ma (MSWD = 0.82). This age is consistent with the Variscan magmatism in the Ossa Morena Zone, and probably also with the high temperature metamorphism of the Valuengo area (Apraiz and Eguiluz 2002).

The results obtained on three titanite crystals are reported in Table 3, with a concordia age of 336.06 ± 1.2 Ma (MSWD = 1.16; Fig. 13). The high closure temperatures of the U–Pb system in titanite allows them to withstand resetting under metamorphic events of up to 750 °C (Spencer et al. 2013). The titanite age is slightly younger than the age of the nearby tonalitic intrusion (338.26 ± 0.32 Ma, this work). Based on these results, a possible rehomogenization of the system due to the dated tonalitic intrusion is unlikely.

The age from the titanite is in broadly accordance with the published Sm–Nd age of 334 ± 32 Ma (Darbyshire et al. 1998) for the Colmenar mineralization and reinforces the evidences of a Variscan-age mineralizing hydrothermal system, consistent with the age and crystallization of regional Variscan magmatism.

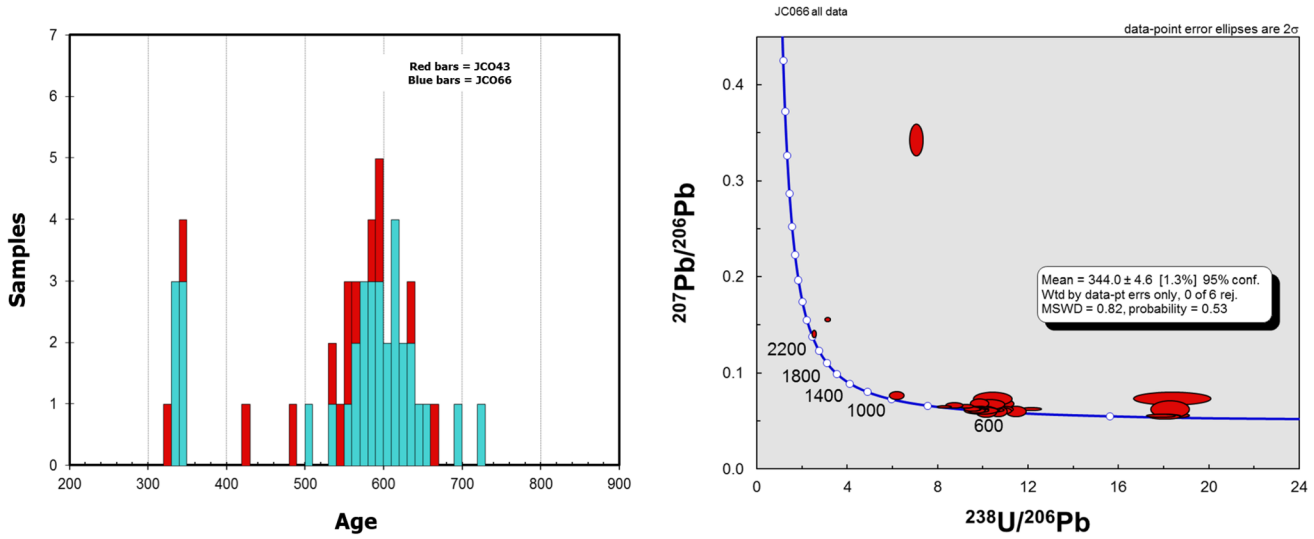

Fig. 12 Histogram and Tera Wasseburg plot (JCO66) showing the age distribution from samples analyzed by SHRIMP corresponding to the albite-magnetite dykes and the attributed value for the obtained Variscan ages

10.2 Ar–Ar dating

The ages obtained over amphiboles related to mineralization at Colmenar are included in Table 4. At JCO62, total released gas age is 335.0 ± 2.4 Ma, although steps 2 to 9 with 66.1% of the released ^{39}Ar define a younger plateau age of 325.2 ± 2.5. This late age overlaps in error with the minimum age obtained for magnetite albite dykes of 326.7 ± 4.6 Ma. In sample JCO72, the total gas age is 349.5 ± 2.1 Ma, although steps 5 to 12 with 65% of the released ^{39}Ar define a plateau age of 338.9 ± 2.1 Ma. These same steps allow defining an isochron age of 335.8 ± 2.0 Ma, considered the most accurate Argon age obtained for the hydrothermal assemblage (Fig. 14). This age coincides within uncertainty with that obtained by U–Pb on titanite of 336.06 ± 1.2 Ma and consistent with the presence of actinolite and titanite in equilibrium.

Geochronological results are consistent with field observations and confirm a temporal relationship between the albitic dykes and the iron-rich mineralization. The actinolite ages are also younger than the age obtained for the foliated tonalite, dated at 338.26 ± 0.32 Ma. This is consistent with the observations that the foliated tonalite, like the Brovales

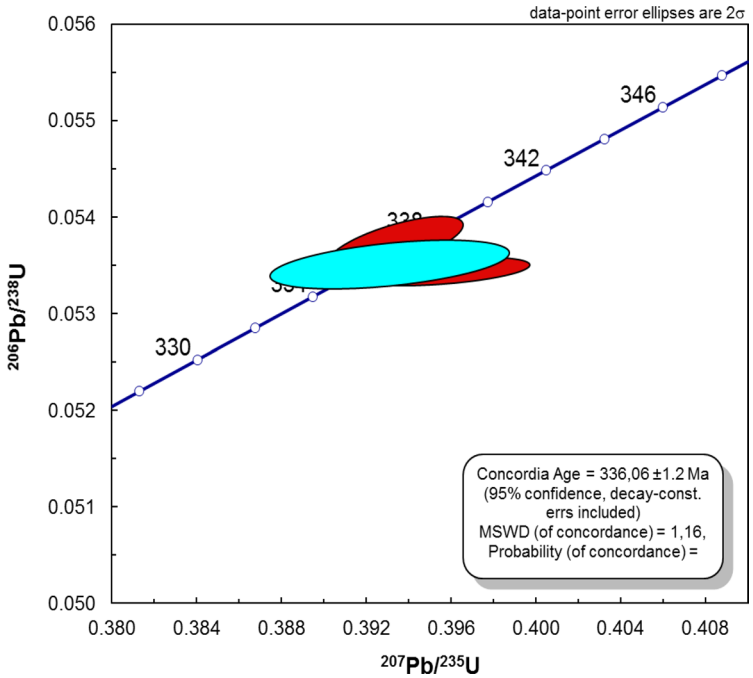

Fig. 13 Concordia age obtained from the three titanite crystals analyzed by TIMS, interpreted as the age of the magmatic—hydrothermal process responsible for the iron mineralization at Colmenar

Pluton, is overprinted by the actinolite-magnetite-rich hydrothermal alteration.

Ages obtained on actinolite could represent the Ar blocking temperatures for a high temperature hydrothermal system or resetting due a high-grade metamorphic event during Variscan times. A graphical summary of best geochronological data obtained for the Colmenar deposit in this work is represented in Fig. 15.

10.3 Rb–Sr and Sm–Nd isotope tracing

The initial Sr ratios obtained for both gabbro samples are similar, (Table 5) with εSr_{340} values of 45 and 39 respectively. These values are the most primitive obtained for the set of samples analyzed in Colmenar and are consistent with a juvenile character on mafic rocks. Regarding the Sm–Nd values, the primitive signature is confirmed for the JCO5 sample, with a positive εNd_{340} value (3.2). Sample JCO4, however, presents a highly negative value εNd_{340} (-11.1), indicative a significantly crustal component than expected for rocks of this nature.

Samples from the eastern tonalite have $^{87}Sr/^{86}Sr_i$ values of 0.70814 and 0.71129 (εSr_{340} = 57 and 102), and consistent with the Nd values (εNd_{340} = −2.6 and −5.7), with a more crustal component than those obtained for the gabbro (JCO5). Similar ranges obtained for the Brovales Pluton, with εNd_{340} values around −5 (Darbyshire et al. 1998; Cambeses et al. 2019) point to a similar source between Brovales pluton and eastern tonalite.

The Rb–Sr results of the albitite in both the dykes and the breccia show similar ratios (Table 4), with εSr_{340} values between 67 and 70 for both types. It was not possible to determine the initial Nd relationships for the breccias given their low concentrations in this element. However, for the dykes, consistent results were obtained with εNd_{340} values of −6.2 and −7.1, pointing to a slightly more pronounced crustal component than those from the Brovales magmatism (Darbyshire et al. 1998). These values deviate from those expected in rocks derived from the fractional crystallization of basaltic magmas or mantle melting, as has been proposed for most of the albitite in the Ossa Morena Zone (Sánchez-García et al. 2008; Etxebarria et al. 2006).

Samples from the mineralization at Colmenar show calculated εSr_{340} values of 59 and 69 respectively. The Nd isotopic composition was determined successfully only in sample JCO45 (εNd_{340} = −15.9), since JCO44 did not present enough amounts of Nd. For comparison, the values obtained for the garnet-rich skarn are similar, with a εSr_{340} of 65 and εNd_{340} of −11.2. These values are not very far from those obtained from lower Cambrian carbonate rocks with εNd_{340} around −9 (Darbyshire et al. 1998) but suggest a higher influence of continental crust.

Darbyshire et al. (1998) measured a εNd_{340} value of −7 for the Colmenar mineralization on a magnetite concentrate, which would coincide with the values obtained for the albitic dykes (−6.2 and −7.1). Likewise, Galindo et al. (1995) obtained similar εNd values between −6 and −6.8 for the magnetite ore replacing tonalite, as well as for a leucogranite and a diorite sample in the deposit. Furthermore, εNd_{340} values of -6 and −8.3 obtained on an albitite from Berrona (unpublished data) are consistent with to those obtained for the Colmenar albitite.

11 Discussion and conclusions

11.1 Analogies with iron oxide copper gold (IOCG) systems

Colmenar mineralization has been interpreted as a skarn (Coullaut et al. 1981; Cuervo et al. 1996; Vázquez et al. 1980; Casquet and Tornos 1991; Sanabria et al. 2005), based on the existence of a calc-silicate coarse-grained hydrothermal assemblage in spatial relationship with an igneous rock (Einaudi et al. 1981). However, other works (Tornos and Casquet 2005; Carriedo and Tornos 2010) proposed that it has more characteristics of an IOCG type system.

This IOCG style of mineralization, initially described by Hitzman et al. (1992), has been cited in various districts such as Carajás in Brazil, Cloncurry, and Gawler Craton in Australia, the Andean IOCG belt in Chile-Peru, the Fennoscandian craton or the Great Bear area in Canada (Williams et al. 2005; Corriveau 2007; Sillitoe 2003; Hitzman et al. 1992; Hitzman 2000; Tallarico et al. 2005; Niiranen et al. 2007).

After the discovery in 1975 of the giant Olympic Dam and given its unique characteristics that did not fit in conventional typologies (Roberts and Hudson 1983), Hitzman et al. (1992) proposed the term of IOCG (Iron Oxide Copper Gold) as a new type of mineralization that has become one of the main prospecting objectives during the last decade. This classification is not restricted to new discoveries, and deposits previously attributed to conventional typologies such as VMS, porphyry copper, skarn or even carbonatites, have been reclassified and included within the IOCG clan (Williams et al. 2005) This deposit type includes giant and significant deposits worldwide such as Salobo, Cristalino, Sossego, Candelaria, Mina Justa, Manto Verde or Ernest Henry among others (Groves et al. 2010).

The general characteristics of this type of mineralization are a matter of debate, and the classification spectrum is somewhat confusing. The most relevant characteristics pointed out to date (Williams et al. 2005; Hitzman et al. 1992; Sillitoe 2003; Corriveau 2007; Richards and Mumin 2013) could be summarized in 6 features: i) Mineralogy

Table 4 Ar/Ar results obtained over amphibole concentrates at Colmenar main mineralization

Step	*T* (C)	*t* (min.)	^{36}Ar	^{37}Ar	^{38}Ar	^{39}Ar	^{40}Ar	%^{40}Ar*	% ^{39}Ar rlsd	Ca/K	^{40}Ar*/^{39}ArK	Age (Ma)	1 s.d
JCO62, Amphibole, 4.80 mg, J = 0.005277 ± 0.43%													
4 amu discrimination = 1.0441 ± 0.51%, 40/39K = 0.0035 ± 78.61%, 36/37Ca = 0.000255 ± 2.11%, 39/37Ca = 0.000665 ± 1.55%													
1	750	12	0.878	2.983	0.868	0.222	258.097	4.5	1.2	66.36420039	53.864104	451.32	45.08
2	850	12	0.096	5.656	0.162	0.185	30.340	20.8	1.0	154.7856606	31.925562	280.89	26.11
3	950	12	0.193	65.571	1.200	1.615	99.018	58.8	8.7	208.619469	36.770568	319.94	3.37
4	990	12	0.174	63.475	1.690	2.167	115.721	69.6	11.7	148.0208997	37.535934	326.03	3.18
5	1020	12	0.219	75.307	1.982	2.699	148.364	68.9	14.6	140.711858	38.557207	334.13	3.91
6	1040	12	0.225	58.206	1.514	2.093	127.587	60.1	11.3	140.2292216	37.077308	322.38	3.42
7	1060	12	0.107	48.252	1.196	1.758	84.985	78.7	9.5	138.3269588	37.690149	327.25	2.92
8	1080	12	0.071	29.199	0.718	1.101	53.646	79.7	6.0	133.4765624	37.092882	322.51	2.92
9	1110	12	0.051	15.800	0.426	0.607	32.961	77.4	3.3	130.9129763	37.651743	326.95	3.03
10	1140	12	0.056	17.515	0.484	0.667	38.549	81.6	3.6	132.1124374	42.474252	364.85	4.08
11	1170	12	0.083	24.228	0.691	1.005	57.291	75.5	5.4	120.9075944	40.738973	351.30	5.23
12	1210	12	0.076	19.347	0.541	0.775	46.132	71.8	4.2	125.358469	40.469465	349.19	4.89
13	1260	12	0.082	14.111	0.370	0.529	38.252	57.2	2.9	134.2839403	37.280860	324.00	5.32
14	1400	12	0.429	83.656	2.261	3.058	225.028	54.8	16.5	137.8518591	40.605901	350.26	3.69
								Cumulative %^{39}Ar rlsd =	100.0		Total gas age =	334.95	2.36
											Plateau age = (steps 4-9) No isochron	326.06	2.71

Step	*T* (C)	*t* (min.)	^{36}Ar	^{37}Ar	^{38}Ar	^{39}Ar	^{40}Ar	%^{40}Ar*	% ^{39}Ar rlsd	Ca/K	^{40}Ar*/^{39}ArK	Age (Ma)	1 s.d
JCO72, Amphibole, 9.18 mg, J = 0.005357 ± 0.48%													
4 amu discrimination = 1.0483 ± 0.48%, 40/39K = 0.0035 ± 78.61%, 36/37Ca = 0.000255 ± 2.11%, 39/37Ca = 0.000665 ± 1.55%													
1	960	12	1.153	12.127	5.413	0.784	379.324	16.0	1.8	138.1731325	78.581396	633.83	21.09
2	990	12	0.364	24.281	2.320	1.576	1600.89	44.8	3.7	137.6029659	45.773794	395.64	4.64
3	1010	12	0.353	43.821	3.245	2.866	1979.82	60.5	6.7	136.5188418	40.888791	357.32	3.61
4	1030	12	0.418	64.192	4.565	4.436	266.416	66.2	10.3	128.9312891	39.542997	346.62	3.17
5	1050	12	0.334	69.774	4.463	4.803	252.090	74.8	11.1	129.4533158	38.910534	341.57	2.91
6	1070	12	0.245	62.416	3.517	4.182	204.466	80.5	9.7	133.1341085	38.568059	338.83	2.86
7	1100	12	0.172	77.682	3.629	5.132	212.177	93.8	11.9	135.0978891	38.106960	335.13	2.63
8	1150	12	0.086	23.513	1.048	1.489	71.420	98.5	3.5	141.1764024	38.083911	334.95	2.77
9	1200	12	0.102	28.559	1.441	1.923	90.965	94.7	4.5	132.4520437	38.391465	337.42	2.86
10	1250	12	0.121	30.219	1.551	1.976	98.401	89.2	4.6	136.5472889	38.757912	340.35	3.04
11	1300	12	0.209	52.272	3.258	3.888	188.757	84.0	9.0	119.4717368	38.888403	341.40	2.77
12	1330	12	0.213	69.486	3.626	4.556	208.639	89.9	10.6	136.1623465	39.026101	342.50	2.82
13	1350	12	0.161	44.818	2.212	2.778	136.786	90.3	6.4	144.3620887	39.868620	349.22	2.76
14	1370	12	0.144	32.078	1.523	1.949	101.753	87.7	4.5	147.3989072	38.597900	339.07	3.65

Table 4 (continued)

Step	*T* (C)	*t* (min.)	^{36}Ar	^{37}Ar	^{38}Ar	^{39}Ar	^{40}Ar	%^{40}Ar*	% ^{39}Ar rlsd	Ca/K	^{40}Ar*/^{39}ArK	Age (Ma)	1 s.d
15	1400	12	0.105	12.467	0.575	0.749	53.068	86.3	1.7	149.1380158	39.736934	348.17	3.40
								Cumulative %^{39}Ar rlsd =	100.0		Total gas age =	349.51	2.13
											Plateau age =	338.86	2.30
											(steps 5-12) Isochron age =	335.80	1.95

Note: isotope beams in mV, rlsd = released, error in age includes J error, all errors 1 sigma (^{36}Ar through ^{40}Ar are measured beam intensities, corrected for decay for the age calculations)

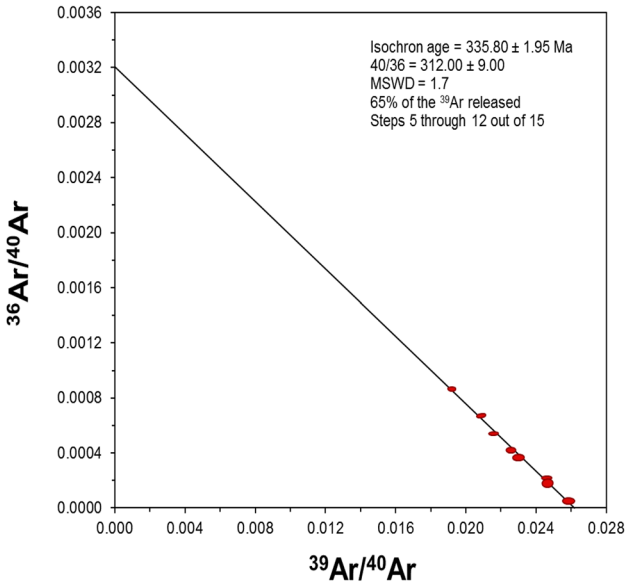

Fig. 14 Isochron age obtained from the plateau steps at sample JCO72, considered as the best result by this method for the age of the mineralization assemblage at Colmenar

with abundant Fe oxides, abundance of Cu-Fe sulfides but poor in pyrite-pyrrhotite; ii) relationship to hydrothermal systems with strong structural control along major crustal scale discontinuities; iii) Absence of clear relationships with magmatic rocks such as those observed for porphyry or skarn systems; iv) relationship with mid to high temperature alterations (400–600 °C) with enrichment in Na (albite-clinoamphibole-diopside), Na-Ca-Fe (magnetite-actinolite-apatite) or K–Fe (potassium feldspar-magnetite-biotite-amphibole); v) Geochemical signature enriched in Cu–Au–Co–Ni–As–Mo–U-(LREE); and, vi) relationship with hypersaline (> 30% NaCl) aqueous fluids.

The main controversy regarding these deposits is the origin of the hypersaline fluids, which are rich in CO_2, poor in H_2S, and relatively oxidized (Hitzman et al. 1992; Williams et al. 2005). Several authors propose a magmatic origin based on arguments such as the proximity to intermediate igneous rock stocks, the presence of magmatic-hydrothermal gaps or the high temperature Na–Ca alteration. These processes are explained by models that involve the exsolution of hydrothermal fluids from specific plutonic rocks such as K-rich granites or other silicate magmas (Sillitoe 2003; Pollard 2000; Hauck 1990), even pointing to analogies with alkaline porphyry-type deposits, locally enriched with magnetite and with an alkali-calcium alteration (Ulrich and Henrich 2002; Tornos et al. 2010). Other authors, however, point to the predominance of non-magmatic fluids, either connate fluids derived from basins or evaporitic sequences that are involved in thermal convection processes (Barton and Johnson 1996, 2000; Haynes 2000; Haynes et al. 1995),

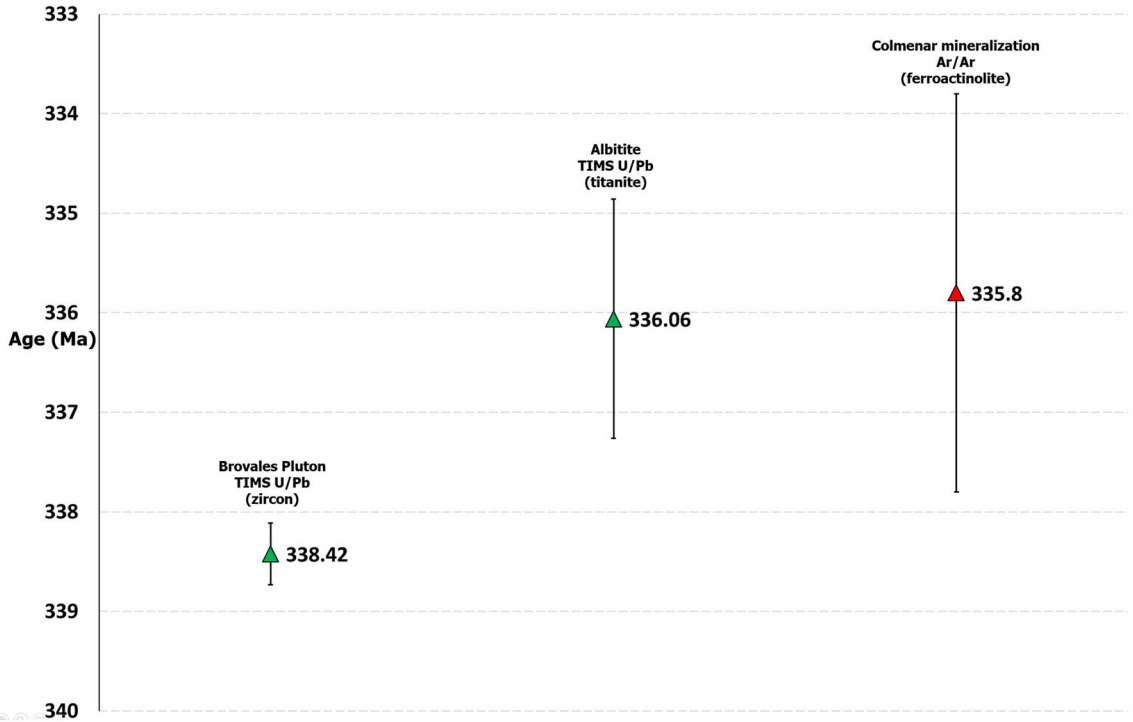

Fig. 15 Comparison summary of the most accurate geochronological ages obtained for the eastern tonalite, the albite-magnetite dykes and the hydrothermal mineralization assemblage. In all cases the ages are within a Variscan range. The albite-magnetite dykes and associated mineralization seem to represent a later event after Brovales intrusion, consistent with observed field relationships. and overlaps with the age of mineralization obtained for Colmenar

or deep metamorphic fluids (Williams 1994; De Jong et al. 1998; Hitzman 2000), which would acquire high salinity during their interaction with Cl-rich rocks, generally evaporites, during their ascent.

IOCG-type deposits are usually spatially associated with the so-called Kiruna-type magnetite-apatite deposits, and the latter have been considered as a subgroup within the IOCG family (Groves et al. 2010; Hitzman et al. 1992; Williams et al. 2005; Corriveau 2007; Sillitoe 2003). Kiruna-type deposits are characterized by the presence of almost monomineralic magnetite masses with local apatite enrichments. They have several common characteristics with IOCG deposits such as the relationship with alkali-calcic alteration. However, they are almost sulfur-free and have very low copper and gold contents.

The mineralization at Colmenar is related with the typical hydrothermal assemblage of IOCG deposits, with an alteration of the alkali-calcium type including alkali feldspar, calcic clinoamphibole and magnetite (Hitzman et al. 1992; Williams et al. 2005), which is perhaps the only variable common to all these deposits. It also bears other characteristics of this style of mineralization such as the relationship with transcrustal structures, a geochemical anomaly in elements such as Co and Ni, the low proportion of sulfides, the abundance of apatite related with a REE enrichment and the relationship with albitite (Na-rich). The structure and texture of the mineralization at Colmenar is very similar to that of the Starra mineralization in the Cloncurry IOCG district (Davidson 1994; Duncan et al. 2014; Mustard et al. 2003; Rotherham 1997; Williams et al. 2001).

11.2 Is albitite a magmatic rock?

Abundant albite rich leucogranite intrusions are widespread across the Ossa Morena Zone, partially hosted by Cambrian volcanic rocks and limestone, especially relevant in the Feria area (Dupont 1979) and the Valuego dome (Coullaut et al. 1981). The albitites conform heterogeneous small intrusions interpreted as linked to processes of fractionation of basaltic magmas (Bellido et al. 2010; Sánchez-García et al. 2003, 2008, 2010*), partial melting of tholeitic gabbro (Etxebarria et al. 2006) or partial melting of crustal rocks (Tomé 2012).

These albitites are commonly related with iron oxide mineralization, such as in La Berrona, La Bóveda, El Soldado, Alfredo, La Valera, Feria or Colmenar (Tornos and Casquet 2005; Carriedo and Tornos 2010). A possibility is that these deposits are

Table 5 Rb–Sr and Sm–Nd results obtained for the different lithologies at Colmenar deposit

Sample	Description	Rb ppm	Sr ppm	Rb/Sr wt	$^{87}Rb/^{86}Sr$	$^{87}Sr/^{86}Sr$	$^{87}Sr/^{86}Sr_{340}$	εSr_{340}	Sm ppm	Nd ppm	Sm/Nd	$^{147}Sm/^{144}Nd$	$^{143}Nd/^{144}Nd$	$^{143}Nd/^{144}Nd_{340}$	εNd_{340}
JCO-1	Tonalite	71.6	311.0	0.2302	0.6663	0.711365	0.708141	57	5.568	25.527	0.2181	0.1319	0.512361	0.512068	− 2.6
JCO-7	Tonalite	13.6	345.2	0.0394	0.1140	0.711844	0.711292	102	7.000	24.800	0.2823	0.1706	0.512290	0.511910	− 5.7
JCO-4	Gabbro	17.8	694.5	0.0256	0.0742	0.707609	0.707081	45	11.900	22.100	0.5385	0.3255	0.512491	0.511425	− 15.1
JCO-5	Gabbro	23.1	691.2	0.0334	0.0967	0.707303	0.706615	39	5.947	25.514	0.2331	0.1409	0.512620	0.512158	− 0.8
JCO-43	ab + mt	16.5	288.6	0.0572	0.1654	0.709608	0.708808	67	3.307	12.381	0.2671	0.1615	0.512239	0.511880	− 6.2
JCO-66	ab + mt	15.7	271.5	0.0578	0.1673	0.709821	0.709011	70	2.611	8.849	0.2951	0.1784	0.512236	0.511839	− 7.1
JCO-44	mt + ab + act	1.5	18.8	0.0798	0.2309	0.709369	0.708252	59	0.710	X	X	X	X	X	X
JCO-45	mt + ab + act	0.6	58.8	0.0102	0.0295	0.709134	0.708991	69	10.400	16.700	0.6228	0.3765	0.512224	0.511386	− 15.9
JCO-46	garnetite	12.3	131.1	0.0938	0.2715	0.709987	0.708673	65	8.100	21.700	0.3733	0.2256	0.512127	0.511624	− 11.2
JCO-47	albite bx	18.6	1627.8	0.0114	0.0330	0.709025	0.708865	68	5.850	X	X	X	X	X	X

Inital and epsilon values calculated for a 340 Ma age, as an aproximation to the age of the deposit. Some samples didn´t provide Sm/Nd ratios due their low Nd concentrations

exhalative in origin (Dupont 1979) and related to the Cambrian alkaline volcanism with which subvolcanic intrusions of albitite could be associated (Bellido et al. 2010; Sánchez-García et al. 2003, 2008, 2010). However, some of these deposits postdate albitites, since they form breccias including fragments of albitite or albitite is replaced by the IOCG-like mineralization (Carriedo and Tornos 2010; Tomé 2012).

Examples of albitites are found in various geological environments, as plagiogranites in ophiolitic sequences (Floyd et al. 1998; Koepke et al. 2004), high-grade metamorphic zones with partial melting of crustal rocks, alkaline complexes, or extremely differentiated magmas in relation to post- to syn-orogenic felsic magmatism (Schwartz 1992; Azer et al. 2010). The origin of albitites, in particular whether they are magmatic or hydrothermal in origin, is the subject of debate (Kovalenko 1978; Chauris 1985; Hitzman et al. 1992; De Jonh and Williams 1995; Williams 1994; Barton and Johnson 1996; Bachiller et al. 1996; Sillitoe 2003; Oliver et al. 2004; Castorina et al. 2006; Corriveau 2007; Tomé 2012).

In many cases, part or all the albitite is of hydrothermal origin and related to (auto-)metasomatic processes with circulation of hypersaline fluids rich in Na and CO_2 at temperatures above 400–500 °C (Mark and Oliver 2006; Oliver et al. 2004). Some experimental studies show that at high temperatures magmatic fluids in equilibrium with two feldspars tend to increase the Na/(Na + K) ratio and form albite when they have high contents of volatiles (including CO_2), and K-feldspar when they are predominantly aqueous (Lagache and Weisbrod 1977; Orville 1963; Pollard 2001). These processes have been proposed for albitites found in stocks or dikes associated with peraluminous granite intrusions (Charoy and Pollard 1989; Barton 1987; Schwartz 1992) or in alteration zones associated with carbonatites (Woolley 1982). Similar processes of hydrothermal albitization have also been mentioned in Cu–(Au) deposits related to alkaline porphyries (Dilles et al. 2000). Although fluids capable of producing a high temperature sodic alteration are generally magmatic, their origin is more controversial in IOCG systems, where the fluids could be either magmatic or connate (Barton and Johnson 1996; Dilles et al. 2000; Pollard 2006).

Metasomatic albitite has been described in proximity of the Burguillos del Cerro Plutonic Complex (Bachiller 1996), as an alteration associated with swarms of leucrogranite dikes hosting quartz veins enriched in gold. Based on fluid inclusion studies, it has been suggested that this albitite was formed by mixing processes between hypersaline magmatic fluids and low salinity meteoric fluids related to discrete episodes of hydraulic fracturing under gradual regional cooling conditions (Bachiller 1996). The leucogranites have been dated by Rb–Sr at 337.2 ± 6.7 Ma (Bachiller 1996).

Tomé (2012) studied in detail the La Berrona albitite intrusion and related magnetite mineralization, both located on the eastern margin of the Brovales Pluton. Through the

study of melt inclusions in quartz phenocrysts, she showed that this albitite is a primary magmatic rock and that its crystallization produced the exsolution of iron-rich hydrothermal fluids that produced the mineralization.

Several arguments indicate that the albitite at Colmenar is of magmatic origin and formed during the partial melting of the host volcano-sedimentary sequence: (i) transition of dykes and albitite breccias to diatexitic zones with domains of albitic leucosome in volcano-sedimentary rocks with intercalations of primary magnetite; (ii) the presence of magmatic textures such as UST growths, magmatic foliation, and myrmekitic or pegmatitic textures; (iii) absence of an appreciable hydrothermal alteration selvage around the dykes, which have sharp intrusive contacts; (iv) coexistence with leucogranite showing textures suggesting melt immiscibility; (v) oxygen isotope equilibrium temperatures of 640–720 °C consistent with the metamorphic conditions identified in the area (Apraiz and Eguiluz 1996); (VI) a magmatic origin for similar albitites in the Valuengo Dome (Tomé 2012).

The albitite at Colmenar seem to be related to local anatexis of rocks with unusual composition, including iron rich exhalites. Anatexis is interpreted as coeval with the high temperature-low pressure metamorphism that took place during the formation of the Valuengo Dome during Variscan extension. This Variscan metamorphism has been interpreted (Tornos and Casquet 2005) as associated with orogenic collapse and intrusion of a deep mafic complex (Simancas et al. 2003), as ultimately the responsible for anatexis.

Sr and Nd signatures on albitites at Colmenar match values with other crustal-derived variscan magmas at the Ossa Morena Zone (Fig. 16, Darbyshire et al. 1998, Casquet et al. 2001, Cambeses 2015). This observation and the match of the inherited zircon population on this magmas with the Ossa-Morena basement zircon ages (Pereira et al. 2011) reinforces the petrogenetic link between the albitite and basement rocks.

Perhaps, high content in fluxing elements (F-P) of the exhalative horizons has played a major role in the formation of the albitite and mineralization by depressing the solidus temperature of the system and displacing the eutectic point towards the albite apex. High concentrations of F-P have been identified in the apatite-rich domains in the leucosomes at Colmenar, large amounts of fluorite in the stratabound Soldado mine or of B at the Monchi mine (Tornos and Casquet 2005; Carriedo and Tornos 2010).

Las Mayorgas Formation includes levels enriched in scapolite (Vázquez et al. 1980), that has been used as an indicator for the presence of metaevaporites (Edfelt et al. 2005; Pan 1998). At regional scale, the Early Cambrian limestone has abundant indicators of deposition in a tidal to subtidal environment that can host evaporites (Perejon and Moreno-Eiris 1992; Álvaro et al. 2000). Partial melting of evaporitic levels within the metamorphosed sequence could be another source of fluxing elements. They could also be the source of chlorine, critical for the efficient transport of Fe as chloride complexes (Barton and Johnson 1996), and the source of the sodium that stabilizes albite.

11.3 Albitic magmas and IOCG type hydrothermalism

A characteristic of IOCG systems is their relationship with large trans-crustal structures favoring circulation of deep hydrothermal fluids of unclear origin responsible for the alkali-calcium alteration and the iron mineralization. In the case of Colmenar, geological evidence suggests that similar fluids are of magmatic-hydrothermal origin and related with the exsolution of fluids during the crystallization of the albitic melts (Fig. 16).

The εNd_{340} results of the mineralization and albitite at Colmenar, between −15.9 and −6.0, are more negative than those of the Brovales Pluton (−2.6 and −5.7) or the gabbro (+3.2) suggesting that fluids where not in equilibrium with these intrusions but with more crustal sources.

Zircon dating of the albite-magnetite dikes has given a peak age range between 540 and 640 Ma, with few older ages that could reflect the existence of zircons derived from a Paleoproterozoic basement (Fernández et al. 2002).

This age range would coincide with subduction-related magmatic activity development of a magmatic arc in the northern margin of Gondwana, between 540–560 and 620–650 Ma (Fernández et al. 2002). The hanging wall of the Malcocinado Formation, in which the Las Mayorgas Formation is correlated, is dated at around 542 Ma (López-Guijarro et al. 2008). This would indicate that practically all the zircon grains would be inherited from the host sequence.

There is a significant time gap between these ages and a minor set of clearly Variscan ages (349.7 ± 5.1 to 326.7 ± 4.6 Ma; Fig. 12) found in poorly developed rims of some zircon grains. A more accurate age for these albite magmas has been obtained by U–Pb TIMS on titanite, yielding an age of 336 ± 1.2 Ma, and overlapping with the three youngest SHRIMP U–Pb ages of the albite-magnetite dikes. This indicates that the youngest magmatic crystallization event of the albitite at Colmenar was Variscan and contradicts that of nearby albitite intrusions, which have been interpreted as Cambrian (Sánchez-García et al. 2008).

Our interpretation is that due to high F activities, the albitite was slightly undersaturated in zirconium and zircon was only locally able to precipitate over inherited old zircon grains from the source. Cathodoluminiscence images of zircons from La Berrona (Carriedo unpublished data) reveal the presence of inherited cores and complex internal textures. Corrosion and dissolution textures are also observed at discrete zircon grains supporting a subsaturated zirconium composition of albitite there. Thus, it is possible that other albitite bodies of the region, dated as Cambrian, could also

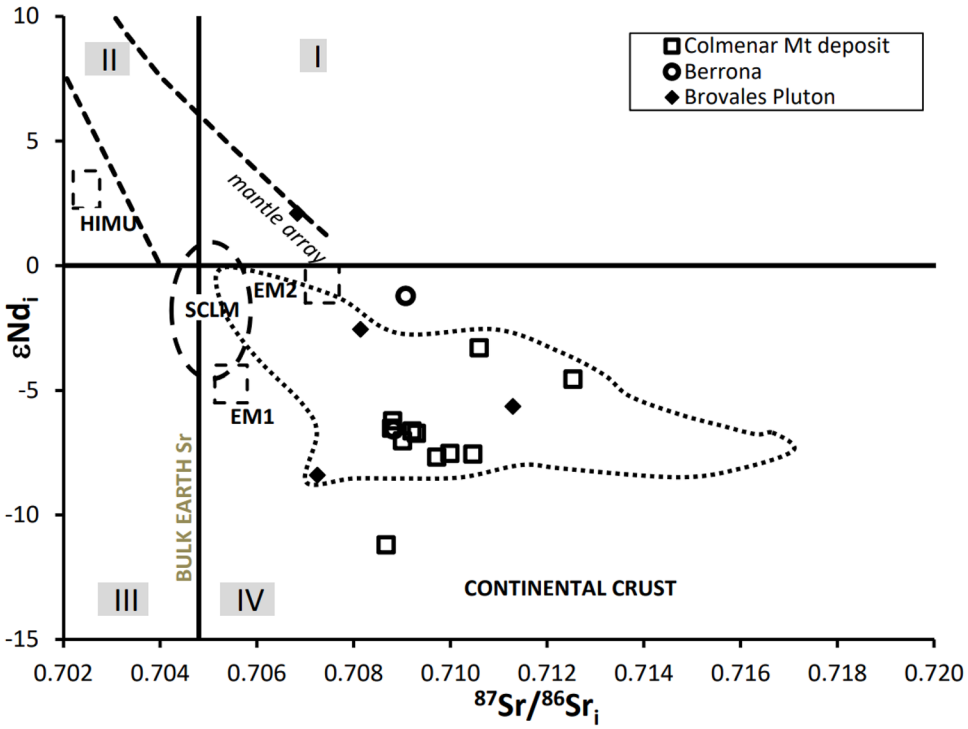

Fig. 16 $^{87}Sr/^{86}Sr$ vs εNdi diagram showing the isotopic similitudes between the mineralization at Colmenar and the Variscan plutonic rocks at the Ossa Morena Zone. The field of Variscan igneous rocks (dotted line) is from Casquet et al. (2001), Cambeses (2015), Tornos et al. (this volume) and Darbyshire & Galindo (unpub. data)

be Variscan in age. This interpretation is also consistent with the Ar–Ar Variscan ages of La Berrona mineralization (Carriedo unpublished data).

A first attempt of dating the mineralization was an Sm–Nd isochrone of a magnetite concentrate, that yielded a Variscan age of 334 ± 32 Ma (Darbyshire et al. 1998), consistent with the Ar–Ar isochron age in this work (335.8 ± 2 Ma). These ages correspond to the main IOCG type hydrothermal activity or the last thermal peak, overlapping in error with the albitite ages.

The eastern tonalite has a robust concordia age of 338.42 ± 0.31 Ma, constraining the age range and accuracy for previous Variscan ages attributed to Brovales Pluton magmatism (ca 340 7 Ma; Montero et al. 2000; Cambeses 2015). This accuracy points to that at Colmenar this calc-alkaline magmatism slightly predates the formation of albitite and mineralization.

The low contents of copper and gold in the Colmenar mineralization may be due to different factors like the high solubilities of these elements in high temperature hydrothermal fluids, the lack of reduced sulfur or that the fluid was simply poor in Cu and Au. The solubility of metals transported as chlorides is highly dependent on temperature (Brimhall and Crerar 1987; Crerar et al. 1985) and high solubility at high temperatures makes it impossible to precipitate them at temperatures above 450 °C. Therefore, if the Colmenar hydrothermal system formed at high temperatures and there is no overprint of late, low temperature, hydrothermal superposition it is unlikely that Cu–Au ores could form. The presence of pyrite suggests that the reduced sulfur content was not the limiting factor.

The $\delta^{34}S$ values of pyrite (15–19‰; Cuervo et al. 1996) are significantly higher than those of sulfur of juvenile origin (0 ± 3‰; Ohmoto 1986) but fully compatible with a derivation of the reduced sulfur from the host rocks, either via anatexis and incorporation into the magmatic-hydrothermal fluid, or by hydrothermal leaching of host rocks (Cuervo et al. 1996). The high temperatures, ductile deformation and proximity to the albitites responsible for fluid exolution points Colmenar to be the root of an IOCG like system with limited fluid rock interaction. However, the migration along major variscan structures of those fluids with more effective hydrothermal leaching of host rocks could favor their sulphur and metal enrichment, capable to generate distal Cu–Au rich end members under appropriate conditions.

12 Conclusions

Geological observations suggest that the Colmenar deposit was formed by an epigenetic hydrothermal process, from Na–Ca–Fe-rich fluids replacing Ca-Al-Si-bearing rocks (calc-silicate hornfels) by an assemblage with albite, actinolite and magnetite, characteristic of IOCG systems. Geological, geochemical and geochronological relationships suggest that the ore-forming fluids derived from the crystallization of an albite ± magnetite magma produced during the anatexis of country rocks at Variscan times (Fig. 16).

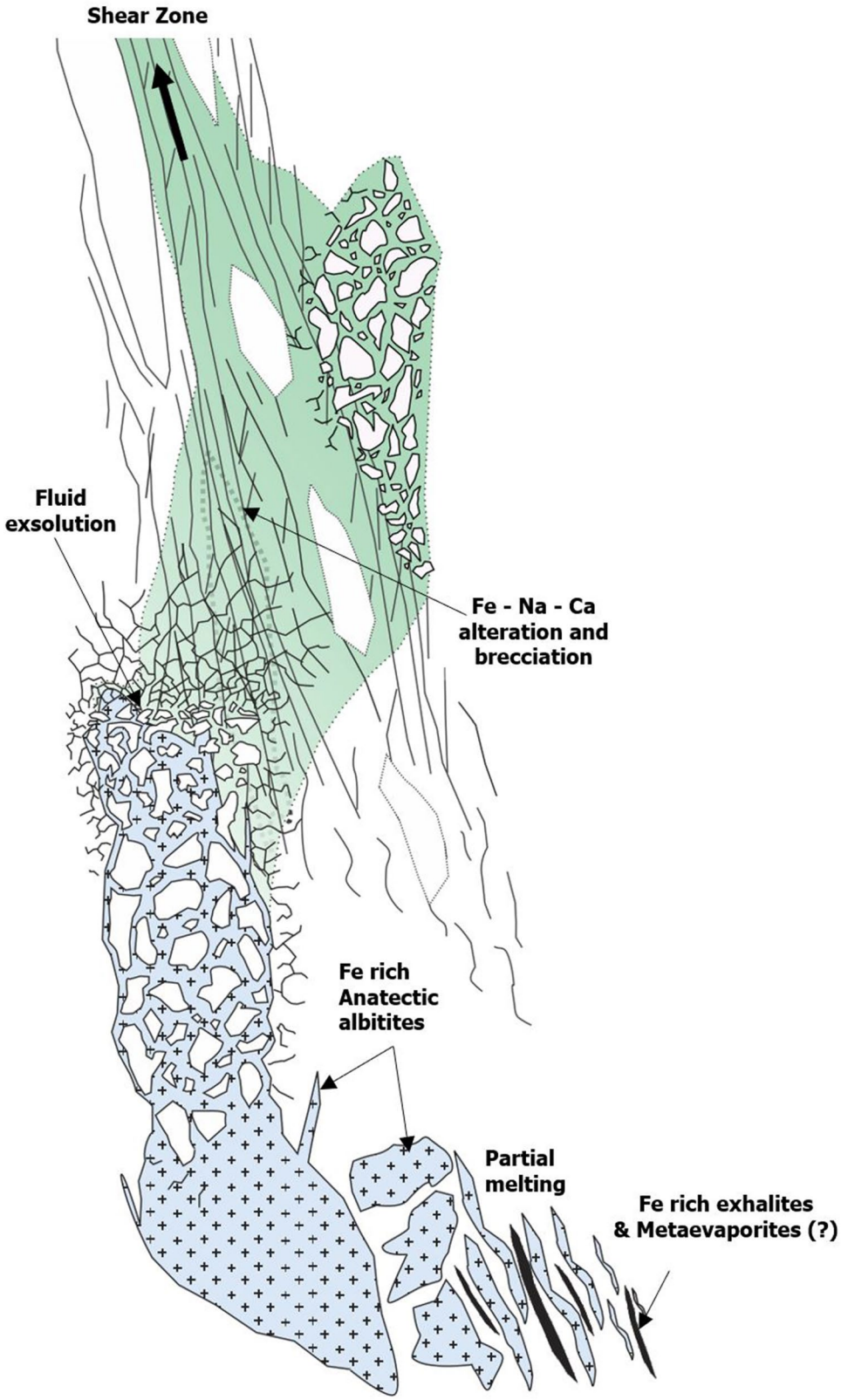

Fig. 17 Summary sketch of magmatic hydrothermal processes on the genesic model for Colmenar, supported by the field observations and isotopic results.

Cambrian mineralization interbedded in the host rocks points as responsible for iron enrichment during partial melting processes, generating albitic magmas with textural domains composed by equilibrium textures of albite-magnetite, coexisting with Quartz and K-feldspar iron poor domains. Transition between both is sharp and does not show reaction borders or disequilibrium textures, pointing to magmatic immiscibility processes between both phases (Fig. 17).

These albitic magmas exsolved an hydrothermal iron-rich phase, responsible for the main mineralization and related sodic-calcic alteration at the deposit, with field observations supported by Nd isotope geochemistry. These fluids channelized along a ductile–brittle shear zone, replace carbonate-rich rocks, developing a prograde alteration dominated by magnetite, ferroactinolite and albite.

The age of the albitic magmas is 336 ± 1.2 Ma (U–Pb titanite) and synchronous with ages from the IOCG mineralization (335.8 ± 2 Ma; Ar–Ar amphibole). Both processes are slightly younger than the emplacement of the Brovales pluton (338.42 ± 0.31 Ma), and consistent with the evidences of post-cooling iron-rich hydrothermal alteration affecting it.

A link is established between high temperature Variscan metamorphism and mineralization at Colmenar. This metamorphism could be partially related with a post-magmatic relaxation/extension during the cooling of the Brovales pluton, favouring decompression and fluid circulation. The high volatile content of the sedimentary sequence, suggested by the abundance of apatite, could decrease the melting point of the iron-rich host rocks, favouring partial melting processes and the genesis of albite-magnetite magmas. During cooling, these magmas could exsolve sodium- and iron-rich fluids, which reacted with the carbonate-rich rocks producing a characteristic alteration of magnetite, ferroactinolite and albite mainly developed along a shear zone, where fluid circulation was more relevant.

Exploration criteria for IOCG deposits at Ossa Morena could include the coexistence of extensional zones linked with Variscan major structures, the presence of distal albitic intrusions associated with high-grade metamorphic grades, and the occurrence of former (Cambrian) stratabound orebodies within the host rock sequence.

In contrast with most IOCG deposits, where the origin of the fluids remains unknown, in Colmenar we could establish a relationship between fluids and albitic melts derived from partial melting processes of volcanosedimentary rocks. This might provide a metallogenetic model that could be tested in other analogous IOCG belts worldwide.

Acknowledgements This paper is a tribute to Dr Carmen Galindo, who passed away in 2019. This work was supported by project RTI2018-099157-A-I00 and grant programs from the Spanish Geological Survey (IGME), the Society of Economic Geologists (SEG) and Swiss funds (FNSNF). Would like to thank Cesar Casquet, Francisco Velasco, Cristina Tome, Christopher Heinrich and Cecilio Quesada for the fruitful discussions at the field. We acknowledge the support from Luis Fontbote, Urs Schaltegger, Richard Spikings, Maria Ovtcharova & Kalin Kouzmanov during the analytical stage at the Earth Science Department at Geneva´s Universtity, and Nycole Rayner for her shared experiences during SHRIMP analysis at Canadian Geological Survey in Ottawa. Thanks for Jose Manuel Fuenlabrada for his expertise at the analytical stage at the Geochronology Unit from Complutense University of Madrid. Finally, we thank to Aitor Cambeses, and Antonio Castro for their review and suggestions for the improvement of this paper.

References

Abalos Villaro, B., Gil Ibarguchi, I., & Eguiluz, L. (1991). Structural and metamorphic evolution of the Almaden de la Plata Core (Seville, Spain) in relation to syn-metamorphic shear between the Ossa-Morena and South Portuguese zones of the Iberian Variscan fold belt. *Tectonophysics, 191*(3–4), 365–387.

Álvaro, J. J., Rouchy, J. M., Bechstädt, T., Boucot, A., Boyer, F., Debrenne, F., et al. (2000). Evaporitic constraints on the southward drifting of the western Gondwana margin during Early Cambrian times. *Palaeogeography, Palaeoclimatology, Palaeoecology, 160*(1–2), 105–122.

Apraiz, A. (1998). *Geología de los Macizos de Lora del Río y Valuengo (Zona de Ossa Morena). Evolución tectometamórfica y significado geodinámico* (p. 575). Spain: Universidad del País Vasco.

Apraiz, A., & Eguiluz, L. (1996). El núcleo metamórfico de Valuengo (Zona de Ossa Morena, Macizo Ibérico): petrografía, termobarometría y evolución geodinámica. *Revista de la Sociedad Geológica de España, 9*(1–2), 29–49.

Apraiz, A., & Eguiluz, L. (2002). Hercynian tectono-thermal evolution associated with crustal extension and exhumation of the Lora del Rio metamorphic core complex (Ossa-Morena zone, Iberian Massif, SW Spain). *International Journal of Earth Sciences, 91*(1), 76–92.

Arenas, R., Díez-Fernández, R., Rubio-Pascual, F. J., Sánchez-Martínez, S., Martín-Parra, L. M., Matas, J., et al. (2016). The Galicia–Ossa-Morena zone: proposal for a new zone of the Iberian Massif. Variscan implications. *Tectonophysics, 681,* 135–143.

Azer, M. K., Stern, R. J., & Kimura, J. (2010). Origin of a Late Neoproterozoic (605 ±13 Ma) intrusive carbonate-albitite complex in Southern Sinai, Egypt. *International Journal of Earth Sciences, 99,* 245–267.

Bachiller, N. (1996). Las alteraciones hidrotermales de los leucogranitos del Complejo intrusivo de Burguillos del Cerro (Badajoz). Edad, geoquímica y modelo de procedencia y evolución de los fluidos. *Master Thesis, Universidad Complutense de Madrid, Madrid*, p. 151

Bachiller, N., Quílez, E., Casquet, C., & Galindo, C. (1996). Albititas metasomáticas y venas de cuarzo en los leucogranitos de Burguillos del Cerro (España). Modelo de evolución hidrotermal basado en el estudio de inclusiones fluidas. *Geogaceta, 20,* 1504–1506.

Baeza, L., Ruiz, C., & Ruiz, M. (1978). Presencia de formaciones volcanosedimentarias y mineralizaciones de hierro asociadas en el eje magmático La Coronada-Villaviciosa (Córdoba). *Boletín Geológico Minero, 89–5,* 431–437.

Bard, J., & Moine, B. (1979). Acebuches amphibolites in the Aracena hercynian metamorphic belt (southwest Spain): geochemical variations and basaltic affinities. *Lithos, 12*(4), 271–282.

Barton, M. D. (1987). Lithophile element mineralization associated with Late Cretaceous two-mica granite in the Great Basin. *Geology, 15,* 337–340.

Barton, M. D., & Johnson, D. A. (1996). An evaporitic source model for igneous-related Fe oxide-(REE-Cu-Au-U) mineralization. *Geology, 24,* 259–262.

Barton, M. D., & Johnson, D. A. (2000). Alternative brine sources for Fe-Oxide (-Cu-Au) systems: Implications for hydrothermal alteration and metals. In: T. M. Porter (Ed.) *Hydrothermal iron oxide copper–gold and related deposits: a global perspective* (pp. 43–60).

Bellido, F., Diez-Montes, A., & Sánchez-García, T. (2010). Caracterización geoquímica y estudio comparativo de plagiogranitos de las Zonas Surportuguesa y Ossa Morena (SO del Macizo Ibérico, España). *Estudios Geologicos, 66*.

Belousova, E. A. (2006). Zircon crystal morphology, trace element signatures and hf isotope composition as a tool for petrogenetic modelling: examples from Eastern Australian Granitoids. *Journal of Petrology, 47*(2), 329–353.

Breiter, K., Müller, A., Leichmann, J., & Gabasova, A. (2005). Textural and chemical evolution of a fractionated granitic system: the Podlesi stock, Czech Republic. *Lithos, 80,* 323–345.

Brimhall, D. H., & Crerar, D. (1987). Ore fluids: magmatic to supergene. *Reviews Mineralogy, 17,* 235–321.

Cambeses, A. (2015). Ossa-Morena Zone Variscan 'calc-alkaline' hybrid rocks: interaction of mantle- and crustal-derived magmas as a result of intra-orogenic extension-related intraplating. (Ph D), University of Granada.

Cambeses, A., Scarrow, J. H., Montero, P., Lázaro, C., & Bea, F. (2017). Palaeogeography and crustal evolution of the Ossa-Morena Zone, southwest Iberia, and the North Gondwana margin during the Cambro-Ordovician: a review of isotopic evidence. *International Geology Review, 59*(1), 94–130. https://doi.org/10.1080/00206814.2016.1219279.

Cambeses, A., Montero, P., Molina, J., Hyppolito, T., & Bea, F. (2019). Constraints of mantle and crustal sources and interaction during orogenesis: a zircon SHRIMP U-Th-Pb and O isotope study of the 'calc-alkaline'Brovales pluton, Ossa-Morena Zone, Iberian Variscan Belt. *Lithos, 324,* 661–683.

Carriedo, J., & Tornos, F. (2010). The iron oxide , copper–gold belt of the Ossa-Morena Zone, southwest Iberia: implications for IOCG genetic models. In: Porter T.M. (Ed.) *Hydrothermal iron oxide copper–gold and related deposits: a global perspective, 4* (pp. 441–460).

Casquet, C., & Tornos, F. (1991). Influence of depth and igneous geochemistry on ore development in skarns: The Hercynian Belt of the Iberian Peninsula. *Skarns, their petrology and metallogeny. Augustithis, Athens* (pp. 555–591).

Casquet, C., Galindo, C., Tornos, F., & Velasco, F. (2001). The aguablanca Cu-Ni ore deposit (Extremadura, Spain), a case of synorogenic orthomagmatic mineralization: Isotope composition of magmas (Sr, Nd) and ore (S). *Ore Geol Rev*, *18*, 237–250.

Castorina, F., Masi, U., Padalino, G., & Paomba, M. (2006). Constraints from geochemistry and SR-Nd isotopes for the origin of albitite deposits from Central Sardinia (Italy). *Mineralium Deposita, 41,* 323–338.

Charoy, B., & Pollard, P. J. (1989). Albite-rich silica-depleted metasomatic rocks at Emuford, northeast Queensland: Mineralogical, geochemical and fluid inclusion constraints on hydrothermal evolution and tin mineralization. *Economic Geology, 84,* 1850–1874.

Chauris, L. (1985). Premiéres donnes géochemiques sur les albitites metasomatiques des invirons de Brest. *Bull Soc Géol Fr., 8,* 885–889.

Chiaradia, M., Vallance, J., Fontboté, L., Stein, H., Schaltegger, U., Coder, J., et al. (2009). U-Pb, Re-Os, and $^{40}Ar/^{39}Ar$ geochronology of the Nambija Au-skarn and Pangui porphyry Cu deposits, Ecuador: implications for the Jurassic metallogenic belt of the Northern Andes. *Mineralium Deposita, 44,* 371–387. https://doi.org/10.1007/s00126-008-0210-6.

Chichorro, M., Pereira, M., Diaz-Azpiroz, M., Williams, I., Fernández, C., Pin, C., & Silva, J. B. (2008). Cambrian ensialic rift-related magmatism in the Ossa-Morena Zone (Évora–Aracena metamorphic belt, SW Iberian Massif): Sm–Nd isotopes and SHRIMP zircon U-Th–Pb geochronology. *Tectonophysics, 461*(1–4), 91–113.

Corfu, F., Hanchar, J. M., Hoskin, P. W. O., & Kinny, P. (2003). Atlas of zircon textures. *Reviews in Mineralogy and Geochemistry, 53,* 469–500. https://doi.org/10.2113/0530469.

Corriveau, L. (2007). Iron Oxide Copper-Gold (Ag-Nb-P-REE-U) Deposits: a canadian perspective. *Mineral deposits of Canada: a synthesis of major deposit-types, district metallogeny, the evolution of geological provinces, and exploration methods, Special publication no, 5,* 307–328.

Coullaut, J. L. (1979). *Geología y metalogenia del criadero de San Guillermo Colmenar, Jerez de los Caballeros* (pp. 1–20). Badajoz. Curso Rosso de Luna: IGME.

Coullaut, J. L., Babiano, F., & Fernández, J. (1980). mineralizaciones de hierro del sureste de españa: Mina la Valera. *Comunicaciones presentadas a las jornadas minerometalúrgicas*.

Coullaut, J. L., Fernández, J., & Aguilar, M. J. (1981). Mapa y memoria explicativa de la hoja 1:50.000 .Nº 875 (Jerez de los Caballeros) del Mapa GeológicoNacional (MAGNA). Madrid: Instituto Geológico y MInero de España (IGME).

Crerar, D., Wood, S., & Brantley, S. (1985). Chemical controls on solubility of ore forming minerals in hydrothermal solutions. *Canadian Mineralogist, 23,* 333–352.

Cuervo, S., Tornos, F., Spiro, B., & Casquet, C. (1996). El origen de los fluidos hidrotermales en el Skarn férrico de Colmenar-Santa Barbara (Zona de Ossa Morena). *Geogaceta, 20,* 1499–1500.

Dallmeyer, R. D., & Quesada, C. (1992). Cadomian vs. Variscan evolution of the Ossa-Morena zone (SW Iberia: field and $^{40}Ar/^{39}Ar$ mineral age constraints. *Tectonophysics, 216,* 339–364.

Darbyshire, D. P. F., Tornos, F., Galindo, C., & Casquet, C. (1998). Sm-Nd and Rb-Sr constraints on the age and origin of magnetite mineralization in the Jerez de los Caballeros iron district of Extremadura, SW Spain. *Chinese Science Bulletin, 43,* 28.

Davidson, G. J. (1994). Hostrocks to stratabound iron-formation-hosted Starra gold–copper deposit, Australia I. Sodic lithologies. *Mineralium Deposita, 29*(3), 237–249.

De Jonh, G., & Williams, P. J. (1995). Giant metasomatic system formed during exhumation of mid crustal Proterozoic rocks in the vicinity of the Cloncurry fault, NW Queesland. *Australian Journal of Earth Sciencies, 42,* 281–290.

De Jong, G., Rotherham, J., Phillips, G. N., & Williams, P. J. (1998). Mobility of rare-earth elements and copper during shear-zone related retrograde metamorphism. *Geologie en Mijnbouw, 76,* 311–319.

Diaz Azpiroz, M. D., Castro, A., Fernández, C., López, S., Caliani, J. F., & Moreno-Ventas, I. (2004). The contact between the Ossa Morena and the South Portuguese zones. Characteristics and significance of the Aracena metamorphic belt, in its central sector between Aroche and Aracena (Huelva). *Journal of Iberian Geology, 30,* 23–51.

Díaz Azpiroz, M., Fernández, C., Castro, A., & El-Biad, M. (2006). Tectonometamorphic evolution of the Aracena metamorphic belt (SW Spain) resulting from ridge-trench interaction during Variscan plate convergence. Tectonics 25(1).

Dilles, J. H., Einaudi, M. T., Proffett, J. M., & Barton, M. D. (2000). Overview of the Yerington porphyry copper district: Magmatic to nonmagmatic sources of hydrothermal fluids, their flow paths, alteration affects on rocks, and Cu-Mo-Fe-Au ores. *Society of Economic Geologists Guide book Series, 32,* 55–66.

Doetsch, J. (1967). La investigación de Magnetitas y los sondeos comprobatorios en el Suroeste de España. *Notas y comprobaciones del IGME, 97,* 41–106.

Duncan, R. J., Hitzman, M. W., Nelson, E. P., & Togtokhbayar, O. (2014). Structural and Lithological Controls on Iron Oxide Copper-Gold Deposits of the Southern Selwyn-Mount Dore Corridor, Eastern Fold Belt, Queensland, Australia. *Economic Geology, 109,* 419–456.

Dupont, R. (1979). *Cadre geologique et metallogenese des gisements de fer du sud de la province de Badajoz (Sierra Morena Occidentale-Spagne)*. PhD Thesis, Inst. Nat. Polyt. Lorraine, 371.

Edfelt, A., Armstrong, M., Smith, M., & Martinsson, O. (2005). Alteration paragenesis and mineral chemistry of the Tjarrojakka apatite-iron and Cu (-Au) ocurrences, Kiruna area, northern Sweden. *Mineralium Deposita, 40,* 409–434.

Eguiluz, L. (1987). *Petrogénesis de rocas ígneas y metamórficas en el Anticlinorio Burguillos-Monesterio*. Macizo Ibérico Meridional: Universidad del Pais Vasco, Bilbao.

Eguiluz, L., Fernández, J., Coullaut, J. L., & Garrote, A. (1983). *Mapa y memoria explicativa de la Hoja 1:50:000, No 897 (Monesterio) del Mapa Geológico Nacional (MAGNA)*. Madrid: Instituto Geológico y MInero de España (IGME).

Eguiluz, L., Ábalos, B., Apraiz, A., & Martínez, L. M. (1992). El núcleo de Valuengo: correlación e implicaciones en la interpretación geodinámica de la Zona de Ossa Morena. *Publicaciones del Museo Geológico de Extremadura, 1,* 67.

Eguiluz, L., Ordoñez, B., Ibarguchi, J. I. G., Apraiz, A., & Ábalos, B. (1999). Superposición de ciclos orogénicos: el ejemplo de la Zona de Ossa-Morena (Macizo Ibérico). *Trabajos de Geología, 21,* 79–96.

Eguiluz, L., Gil-Ibarguchi, J. I., Ábalos, B., & Apraiz, A. (2000). Superposed Hercynian and Cadomian orogenic cycles in the Ossa-Morena zone and related areas of the Iberian Massif. *GSA Bulletin, 112*(9), 1398–1413.

Eguiluz, L., Carracedo, S. M., Sarrionandia, E. F., & Apalategui, O. (2004). Nuevos datos tectono-estructurales del Macizo de Brovales (Antiforma de Olivenza-Monesterio): relación con el cabalgamiento de Monesterio. *Geogaceta, 35,* 83–86.

Einaudi, M. T., Meinert, L. D., & Newberry, R. J. (1981). Skarn deposits. *Economic Geology, 75,* 317–391.

Etxebarria, M., Chalot-Prat, F., Apraiz, A., & Eguiluz, L. (2006). Birth of a volcanic passive margin in Cambrian time: Rift paleogeography of the Ossa-Morena Zone, SW Spain. *Precambrian Research, 147,* 366–386.

Expósito, I. (2000). Evolución estructural de la mitad septentrional de la Zona de Ossa Morena y su relación con el límite Zona de Ossa Morena/Zona Centroibérica. *Universidad de Granada*, 295.

Expósito, I., Simancas, J. F., Gonzalez-Lodeiro, F., Bea, F., Montero, P., & Salman, K. (2003). Metamorphic and deformational imprint of Cambrian-Lower Ordovician rifting in the Ossa-Morena Zone (Iberian Massif, Spain). *Journal of Structural Geology, 25*(12), 2077–2087.

Febrel, T. (1970). Metalogenia de la Hoja núm 875, Jerez de los Caballeros (Badajoz). *Boletín Geológico Minero, 81,* 472–492.

Fernández, J., Coullaut, J. L., & Aguilar, M. J. (1981). Geologic map of Jerez de los Caballeros, hoja 875. *Geologic map of Spain, IGME, scale, 1,* 50000.

Fernández, J., Gutiérrez-Alonso, G., & Jeffries, T. E. (2002). The importance of along-margin terrane transport in northern Gondwana: insights from detrital zircon parentage in Neoproterozoic rocks from Iberia and Brittany. *Earth and Planetary Science Letters, 204,* 75–88.

Floyd, P. A., Yaliniz, M. K., & Goncuoglu, M. C. (1998). Geochemistry and petrogenesis of intrusive and extrusive ophiolitic plagiogranites, Central Anatolian Crystalline Complex, Turkey. *Lithos, 42,* 225–241.

Galindo, C., Casquet, C., Darbyshire, D. P. F., Tornos, F., & Cuevo, S. (1995). Sm-Nd isotope geochemistry and dating of magnetites: A case study from an Fe district in the SW of Spain. *Pasava, Kribek, and Zak, eds., Mineral deposits: Rotterdam, Balkema*, pp. 41–43.

Groves, D. I., Bierlein, F. P., Meinert, L. D., & Hitzman, M. W. (2010). Iron Oxide Copper-Gold (IOCG) Deposits through Earth History: Implications for Origin, Lithospheric Setting, and Distinction from Other Epigenetic Iron Oxide Deposits. *Economic Geology, 105,* 641–654.

Hauck, S. A. (1990). Petrogenesis and tectonic setting of middle Proterozoic iron oxide-rich ore deposits; an ore deposit model for Olympic Dam-type mineralization. *U.S Geological Survey Bulletin, 1931,* 4–39.

Haynes, D. W. (2000). *Iron oxide copper (-gold) Deposits: Their position in the ore deposit spectrum and modes of origin* (pp. 71–90). A Global Perspective: Porter T.M. Hydrothermal Iron Oxide Copper- Gold and Related Deposits.

Haynes, D. W., Cross, K. C., Bills, R. T., & Reed, M. H. (1995). Olympic Dam ore genesis: a fluid mixing model. *Economic Geology, 90,* 281–307.

Hitzman, M. W. (2000). *Iron Oxide-Cu-Au Deposits: What, Where* (pp. 9–25). A Global Perspective: When and Why. Hydrothermal Iron Oxide Copper-Gold & Related Deposits.

Hitzman, M. W., Oreskes, N., & Einaudi, M. T. (1992). Geological characteristics and tectonic setting of Proterozoic iron oxide (Cu-U-Au-REE) deposits. *Precambrian Research, 58,* 241–287.

IGME. (1979). *Investigación de Magnetita en el área de la Berrona* (p. 10608). Ministerio de Industria-Dirección General de Minas: IGME.

IGME. (2006). Mapa metalogenético de la provincia de Badajoz. *Escala, 1*(200000), 192.

Jacobsen, S. B., & Wasserburg, G. J. (1980). Sm-Nd isotopic evolution of chondrites. *Earth and Planetary Science Letters, 50,* 139–155.

Julivert, M., Fontboté, J. M., Ribeiro, A., & Conde, L. A. (1974). Mapa tectónico de la Peninsula Ibérica y Baleares E: 1:1.000.000 y memoria explicativa. *Publicaciones del IGME*, p. 113.

Kober, B. (1986). Whole-grain evaporation for $^{207}Pb/^{206}Pb$ age investigations on single zircons using a duble-filament thermal ion source. *Contributions to Mineralogy and Petrology, 93,* 482–490.

Kober, B. (1987). Single-zircon evaporation combined with Pb + emitter-bedding for $^{207}Pb/^{206}Pb$ age investigations usin thermal ion mass spectrometry and implications to zirconlology. *Contributions to Mineralogy and Petrology, 94,* 63–71.

Koepke, J., Feig, S., Snow, J., & Freise, M. (2004). Petrogenesis of oceanic plagiogranites by partial melting of gabbros: an experimental study. *Contributions to Mineralogy and Petrology, 146,* 414–432.

Kovalenko, N. I. (1978). The genesis of rare metal granitoids and related ore deposits. *Metallization associated with acid magmatism.*, pp. 235–247.

Lagache, M., & Weisbrod, A. (1977). The system: two alkali feldspars KCl-NaCl-H_2O at moderate to high temperatures and low pressures. *Contributions to Mineralogy and Petrology, 62,* 77–101.

Locutura, J., Tornos, F., Florido, P., & Baeza, L. (1990). *Ossa Morena Zone: Metallogeny* (pp. 321–330). In E. Martinez, & R.D. Dallmeyer (Eds.) Pre-Mesozoic Geology of Iberia, Springer Verlag.

London, D. (1992). The application of experimental petrology to the genesis and crystallization of granitic pegmatites. *Canadian Mineralogist, 30,* 499–540.

López-Guijarro, R., Armendáriz, M., Quesada, C., Fernández-Suárez, J., Murphy, B. J., Pin, C., et al. (2008). Ediacaran-Palaeozoic tectonic evolution of the Ossa Morena and Central Iberian zones (SW Iberia) as revealed by Sm–Nd isotope systematics. *Tectonophysics, 461*(1–4), 202–214.

López-Munguira, A., & Nieto, F. (2004). Low-grade metamorphism in the central sector of the Ossa-Morena zone. *Journal of Iberian Geology, 30,* 109–118.

Mark, G., & Oliver, N. H. S. (2006). Mineralogical and chemical evolution of the Ernest Henry Fe oxide–Cu–Au ore system, Cloncurry district, northwest Queensland, Australia. *Mineralium Deposita, 40,* 769–801.

Martinez, F. J. (1974). Estudio petrológico de la parte occidental de la provincia de Salamanca. *Trabajos de geología. Universidad de Oviedo, 7,* 3–59.

Mehner, K. R. (1968). Migmatites and the origin of granitic rocks. *Amsterdam*, 391.

Moita, P., Santos, J. F., & Pereira, M. F. (2009). Layered granitoids: interaction between continental crust recycling processes and mantle-derived magmatism: examples from the Évora Massif (Ossa–Morena Zone, Southwest Iberia, Portugal). *Lithos, 111*(3–4), 125–141.

Montero, P., Salman, K., Bea, F., Azor, A., Expósito, I., & Lodeiro, F., et al. (2000). *New data on the geochronology of the Ossa-Morena Zone, Iberian Massif*. Variscan-Appalachian dynamics: The building of the Upper Palaeozoic basement.

Mustard, R., Baker, T., Williams, P. W., Ulrich, T., Mernagh, L. J., & Ryan, C. G. (2003). Cu-rich brines at the Osborne and Starra deposits: implications for immiscibility in Fe-oxide Cu–Au systems. *Transactions Institution Mining Metallurgy, B112,* 189–191.

Nesen, G. (1981). *Le Modèle exogranite-endogranite à stcokscheider et la métallogénie Sn-W*. Etude des gisements de Fontao et Santa Comba (Galice-Espagne): Spécialité Université Nancy.

Niiranen, T., Poutiainen, M., & Mänttäri, I. (2007). Geology, geochemistry, fluid inclusion characteristics, and U-Pb age studies on iron oxide–Cu–Au deposits in the Kolari region, northern Finland. *Ore Geology Reviews, 30,* 75–105.

Ohmoto, H. (1986). Stable isotope geochemistry of ore deposits. *Reviews in Mineralogy, 16,* 491–560.

Oliver, N. H. S., Cleverly, J. S., Mark, G., Pollard, P. J., Fu, B., Marshall, L. J., et al. (2004). Modeling the role of sodic alteration in the genesis of iron oxide–cooper–gold deposits, Eastern Mount Isa Block, Australia. *Economic Geology, 99,* 1145–1176.

Ordóñez, B. (1998). *Geochronological studies of the Pre-Mesozoic basement of the Iberian Massif : the Ossa Morena zone and the Allochthonous Complexes within the Central Iberian zone* (p. 235). Zurich: Tesis Doctoral University.

Orville, P. M. (1963). Alkali ion exchange between vapor and feldspar phases. *American Journal of Science, 261,* 201–237.

Pankhurst, R. J., & O´nions, R. K. . (1973). Determination of Rb/Sr and $^{87}Sr^{86}Sr$ ratios of some standard rocks and evaluation of X-ray fluorescence spectrometry in Rb-Sr geochemistry. *Chemical Geology, 12*(2), 127–136. https://doi.org/10.1016/0009-2541(73)90110-1.

Pereira, M. F., Chichorro, M., Williams, I. S., Silva, J. B., Fernández, C., Díaz Azpiroz, M., & Castro, A. (2009). Variscan intra-orogenic extensional tectonics in the Ossa-Morena Zone (Évora-Aracena-Lora del Río metamorphic belt, SW Iberian Massif): SHRIMP zircon U-Th-Pb geochronology. *Geological Society, 327,* 215–237.

Pereira, M. F., Chichorro, M., Sola, A. R., Silva, J. B., Sanchez-Garcia, T., & Bellido, F. (2011). Tracing the Cadomian magmatism with detrital/inherited zircon ages by in-situ U-Pb SHRIMP geochronology (Ossa-Morena Zone, SW Iberian Massif). *Lithos, 123*(1–4), 204–217. https://doi.org/10.1016/j.lithos.2010.11.008.

Pereira, M. F., Chichorro, M., Silva, J. B., Ordóñez Casado, B., Lee, J. K. W., & Williams, I. S. (2012). Early carboniferous wrenching, exhumation of high-grade metamorphic rocks and basin instability in SW Iberia: Constraints derived from structural geology and U-Pb and ^{40}Ar-^{39}Ar geochronology. *Tectonophysics, 558–559,* 28–44.

Perejon, A., & Moreno-Eiris, E. (1992). Palozoico Inferior de Ossa Morena. In: J.C. Gutierrez Marco, J. Saavedra y I. Rábano (Eds.) *Paleozoico inferior de Ibero-América* (pp. 557–565). Spain: Universidad de Extremadura

Pin, C., Fonseca, P. E., Paquette, J. L., Castro, P., & Matte, P. (2008). The ca. 350 Ma beja igneous complex: a record of transcurrent slab break-off in the Southern Iberia Variscan Belt? *Tectonophysics, 461,* 356–377.

Pollard, P. J. (2001). Sodic (-calcic) alteration in Fe-oxide-Cu-Au districts: an origin via unmixing of magmatic fluids. *Mineralium Deposita, 36,* 93–100.

Pollard, P. J. (2006). An intrusion-related origin for Cu-Au mineralization in iron-oxide-copper-gold (IOCG) provinces. *Mineralium Deposita, 41,* 179–187.

Pupin, J. P. (1980). Zircon and granite petrology. *Contributions to Mineralogy and Petrology, 73,* 207–220.

Quesada, C. (1992). *Evolución Tectónica del Macizo Ibérico (Una historia de crecimiento por acrecencia sucesiva de terrenos durante el Proterozoico superior y el Paleozoico*, Paleozoico Inferior de Ibero América.

Quesada , C., & Sánchez-García, T. (2002). Cartografia geológica continua de la Zona de Ossa Morena, Escala 1:50.000. Madrid: Instituto Geológico y MInero de España (IGME).

Renne, P. R., Swisher, C. C., Deino, A. L., Karner, D. B., Owens, T. L., & DePaolo, D. J. (1998). Intercalibration of standards, absolute ages and uncertainties in $^{40}Ar/^{39}Ar$ dating. *Chemical Geology, 145*(1–2), 117–152. https://doi.org/10.1016/S0009-2541(97)00159-9.

Richards, J. P., & Mumin, A. H. (2013). Magmatic-hydrothermal processes within an evolving Earth: iron oxide–copper–gold and porphyry Cu–Mo–Au deposits. *Geology, 41,* 767–770.

Robardet, M. (2003). The Armorica microplate: fact or fiction? Critical review of the conncept and contradictory palaeobiogeographical data. *Paleogeography Paleoclimatology Paleoecology, 195,* 125–148.

Roberts, D. E., & Hudson, G. R. T. (1983). The Olympic Dam copper–uranium–gold–silver deposit, Roxby Downs, South Australia. *Economic Geology, 78,* 799–822.

Rotherham, J. F. (1997). A metasomatic origin for the iron oxide Au-Cu Starra orebodies, Eastern Fold Belt. *Mount Isa Inlier. Mineralium Deposita, 32*(3), 205–218.

Ruiz García, C. (1975). Génesis de los depósitos de hierro del Suroeste de la provincia de Badajoz. *Tesis*, 227.

San José, M. A., Herranz, P., & Pieren, A. P. (2004). A review of the Ossa-Morena Zone and its limits. Implications for the definition of the Lusitan-Marianic Zone. *Journal of Iberian Geology, 30,* 7–22.

Sanabria, R., Casquet, C., Tornos, F., & Galindo, C. (2005). Las mineralizaciones ferríferas del coto minero San Guillermo (Jerez de los Caballeros, Badajoz, España). *Geogaceta, 38,* 223–226.

Sánchez-García, T., Bellido, F., & Quesada, C. (2003). Geodinamic setting and geochemical signatures of Cambrian-Ordovician rift-related igneous rocks (Ossa-Morena Zone, SW Iberia). *Tectonophysics, 365,* 233–255.

Sánchez-García, T., Quesada, C., Bellido, F., Dunning, G. R., & González del Tánago, J. (2008). Two-step magma flooding of the upper crust during rifting: The Early Paleozoic of the Ossa Morena Zone (SW Iberia). *Tectonophysics, 461*(1–4), 72–90.

Sánchez-García, T., Bellido, F., Pereira, M. F., Chichorro, M., Quesada, C., Pin, C., et al. (2010). Rift-related volcanism predating the birth of the Rheic Ocean (Ossa-Morena zone, SW Iberia). *Gondwana Research, 17,* 392–407.

Schmid, R., Fettes, D., Harte, B., Davis, E., & Desmons, J. (2007). A systematic nomenclature for metamorphic rocks. *Recomendations by the IUGS Subcommision on the systematics of metamorphic rocks*.

Schwartz, M. O. (1992). Geochemical criteria for distinguishing magmatic and metasomatic albite-enrichment in granitoids—examples from the Ta-Li granite Yichun (China) and the Sn-W deposit Tikus (Indonesia). *Mineralium Deposita, 27*(2), 101–108.

Shannon, J. R., Walker, B. M., Carten, R. B., & Geraghty, E. P. (1982). Unidirectional solidification textures and their significance in determining relative ages of intrusions at the Henderson Mine, Colorado. *Geology, 10,* 293–297.

Sillitoe, R. H. (2003). Iron oxide-copper-gold deposits: an Andean view. *Mineralium Deposita, 38,* 787–812.

Silva, J. B., Oliveira, J. T., & Ribeiro, A. (1990). Structural outline of the South Portuguese Zone. *Martínez, E.,Dallmeyer, R.D. Pre-Mesozoic Geology of Iberia* (pp. 348–362). Berlín: Springer.

Simancas, J. F., Carbonell, R., Gonzalez-Lodeiro, F., Perez Estaun, A., Juhlin, C., Ayarza, P., et al. (2003). Crustal structure of the transpressional Variscan orogen of SW Iberia: Sw Iberia deep seismic reflection profile (IBERSEIS). *Tectonics, 22,* 1063–1078.

Spencer, K. J., Hacker, B. R., Kylander-Clark, A. R. C., Andersen, T. B., Cottle, J. M., Stearns, M. A., et al. (2013). Campaign-style titanite U-Pb dating by laser-ablation ICP: implications for crustal flow, phase transformations and titanite closure. *Chemical Geology, 341,* 84–101.

Stacey, J. S., & Kramers, J. D. (1975). Approximation of terrestrial lead isotope evolution by a 2-stage model. *Earth Planet Sci Lett*, *26*(2), 207–221.

Staudacher, T., Jessberger, E. K., Dorflinger, D., & Kiko, J. (1978). A refined ultrahigh-vacuum furnace for rare gas analysis. *Journal of Physics E*. https://doi.org/10.1088/0022-3735/11/8/019.

Steiger, R. H., & Jäger, E. (1997). Subcomission on geochronology: convention on the use of decay constant in geo and cosmochronology. *Earth and Planetary Science Letters, 36,* 359–362.

Stern, R. A. (1997). The GSC Sensitive High Resolution Ion Microprobe (SHRIMP): analytical techniques of zircon U-Th-Pb age determinations and performance evaluation. *Radiogenic Age and Isotopic Studies, Report 10, Geological Survey of Canada*, pp. 1–31.

Stern, R. A., & Amelin, Y. (2003). Assessment of errors in SIMS zircon U-Pb geochronology using a natural zircon standard and NIST SRM 610 glass. *Chemical Geology, 197,* 11–146.

Tallarico, F. H. B., Figueiredo, B. R., Groves, D. I., Kositcin, N., McNaughton, J., Fletcher, I. R., et al. (2005). Geology and SHRIMP U-Pb Geochronology of the Igarapé Bahia Deposit, Carajás Copper–Gold Belt, Brazil: An Archean (2.57 Ga) Example of Iron-Oxide Cu–Au-(U-REE) Mineralization. *Economic Geology, 100,* 7–28.

Tomé, C. (2012). *Fluid and Melt inclusion study of magmatic-hydrothermal mineralization in the Ossa Morena Zone (SW Spain)* (p. 251). Tesis Doctoral: Universidad de Huelva.

Tornos, F. (1989). *Los skarns y mineralizaciones asociadas del Sistema Central Español: modelo de caracterización petrológica, geoquímica y metalogénica*. Tesis Doctoral: Universidad Complutense de Madrid.

Tornos, F., & Carriedo, J. (2006). La relación de los depósitos de tipo IOCG con intrusiones laminares profundas: el SO de la Península Ibérica. *Actas del XIII Congreso Peruano de Geología*, pp. 796–799.

Tornos, F., & Casquet, C. (2005). A new scenario for related IOCG and Ni-(Cu) mineralization: the relationship with giant mid-crustal mafic sills, Variscan Iberian Massif. *Terra Nova, 17*(3), 236–241.

Tornos, F., Casquet, C., Relvas, J. M. R. S., Barriga, F. J. A. S., & Saez, R. (2002). The relationship between ore deposits and oblique tectonics: the SW Iberian Variscan Belt. The timing and location of major ore deposits in an evolving orogen. *Geological Society of London, 204,* 179–198.

Tornos, F., Casquet, C., & Galindo, C. (2003). Hydrothermal iron oxide (-Cu-Au) mineralization in SW Iberia: Evidence for amultiple origin. In *Proceedings of seventh Biennial SGA Meeting "Mineral Exploration and Sustainable Development", Athens* (pp. 395–398).

Tornos, F., Inverno, C. M. C., Casquet, C., Mateus, A., Ortiz, G., & Oliveira, V. (2004). The metallogenic evolution of the Ossa-Morena Zone. *Journal of Iberian Geology, 30,* 143–181.

Tornos, F., Velasco, F., Barra, F., & Morata, D. (2010). The Tropezón Cu–Mo–(Au) deposit, Northern Chile: the missing link between IOCG and porphyry copper systems? *Mineralium Deposita, 45,* 313–321.

Ulrich, T., & Henrich, C. A. (2002). Geology and alteration gechemistry of the porphyry Cu-Au deposit at Bajo de la Alumbrera, Argentina. *Economic Geology, 96,* 1865–1888.

Vance, J. A. (1961). Polysynthetic twinning in plagioclase. *The American Mineralogist, 46,* 1097–1119.

Vázquez, F., & Fernández, F. (1976). Contribución al conocimiento geológico del Suroeste de España en relación con la prospección de depósitos de magnetitas. *Memoria del Instituto Geológico y Minero de España, 89,* 130.

Vázquez, F., Arteaga, R., & Schemerhorn, J. J. (1980). Depósitos minerales del SO de la Península Ibérica. *Boletín Geológico Minero, 91–2,* 293–342.

Wendt, I., & Carl, C. (1991). The statistical distribution of the mean squared weighted deviation. *Chemical Geology, 86*(4), 275–285. https://doi.org/10.1016/0168-9622(91)90010-T.

Williams, P. J. (1994). Iron mobility during synmetamorphic alteration in the Selwyn Range area, NW Queesland: Implications for the origin of ironstone-hosted Au-Cu deposits. *Mineralium Deposita, 29,* 250–260.

Williams, P. J., Dong, G., Ryan, C. G., Pollard, P. J., Rotherham, J. F., Mernagh, T. P., et al. (2001). Geochemistry of hypersaline fluid inclusions from the Starra Au-Cu deposit, Cloncurry district, Queensland. *Economic Geology, 96,* 875–883.

Williams, P. J., Barton, D. M., Johnson, D. A., Fontboté, L., De Haller, A., Mark, G., et al. (2005). Iron oxide copper–gold deposits: geology, space–time distribution, and possible modes of origin. *Economic Geology, 100,* 371–405.

Woolley, A. R. (1982). A discussion of carbonatite evolution and nomenclature, and generation of sodic and potassic fenites. *Mineralogical Magazine, 46,* 13–17.